Contact-based transfer of thymidylate promotes collective tumor growth

Mohammad A. Siddiqui[1,#], Anne Mette A. Rømer[1,#], Luisa Pinna[1], Vignesh Ramesh[1], Sarah S. Møller[1], Paradesi N. Gollavilli[1], Adriana M. Turtos[1], Steffi Varghese[1], Lærke B. Guldborg[1], Nagendra P. Palani[2], Francesca Napoli[3], Marco Volante[3], Luis Córdova Bahena[4], Marco Velasco[4], Kumar Somyajit[1], Pawel Swietach[5], and Paolo Ceppi[1,7*]

[1]Department of Biochemistry and Molecular Biology, University of Southern Denmark; Odense, Denmark.

[2]Novo Nordisk Foundation Center for Basic Metabolic Research; University of Copenhagen, Denmark.

[3]Department of Oncology, San Luigi Hospital, University of Turin, Italy

[4]Laboratory of Molecular Pharmacology, Faculty of Medicine, National Autonomous University of Mexico, Mexico,

[5]Department of Physiology, Anatomy & Genetics; University of Oxford, UK.

[#]These authors contributed equally

*Correspondence. Email: pceppi@bmb.sdu.dk

Summary. Sustained cell proliferation is a fundamental hallmark of cancer, yet its mechanism remains elusive, particularly in context of heterogenous tumor organization, intercellular interactions, and metabolite exchanges. In this study, we uncover a mechanism of tumor growth via *collective proliferation*, where cells connected by gap junctions enable equilibration of thymidylate (dTMP) to allow the proliferation of cells lacking canonical *de novo* dTMP biosynthesis and salvage driven by thymidylate synthase (*TYMS*) and thymidine kinase 1 (*TK1*) enzymes, respectively. Collective proliferation is driven by dTMP-proficient cancer cells alongside cells of varied origins, such as macrophages and endothelial cells. The mechanism is also observed in clinical samples and is validated in a genetic mouse model of lung cancer harboring dual *Tyms*/*Tk1* tumor-specific knockout, in which tumors grow despite lacking enzymatic dTMP synthesis and tumor progression is opposed by gap junction inhibition. Data further hint that this mechanism is critical driver of tumor pathophysiology, influencing key processes such as senescence, genomic instability and drug resistance. These findings revise the current dogma of ubiquitous nucleotide biosynthesis in each proliferating cancer cell in a tumor and suggest that a programmed dTMP distribution maintains collective tumor growth. This mechanism could be exploited in cancer therapy.

Total Word Count:

Keyword. Collective cell proliferation, thymidylate, dTMP equilibration, pyrimidine metabolism, cancer

Introduction. Sustained cell proliferation, a key cancer hallmark, relies on a continuous supply of nucleotides either through multistep *de novo* biosynthesis or salvage of free nucleosides[1]. The current dogma of tumor growth emphasizes the universal activation of pyrimidine synthesis[2], thereby propagating an energy-exhaustive growth model. However, tumors are genetically heterogeneous entities[3] and cells with undetected levels of critical pyrimidine genes are frequently reported in clinical samples[4,5]. The contribution and significance of these cells in cancer growth has never been identified.

Recent studies have suggested that intercellular genetic heterogeneity, caused by disruption in key metabolic pathway genes, can be compensated by the equilibration of metabolites

between electrically coupled cells forming a syncytium[6]. To investigate if pyrimidines could be shared in a similar way, we investigated proliferation dynamics between cells with active expression of nucleotide metabolism genes and cells with CRISPR/Cas9-mediated ablation of these genes. Strikingly, our findings reveal a compensatory mechanism where cells undergo collective proliferation, mediated by sharing of thymidylate among cells. These results, supported by *in vivo* models and clinical data, challenge the essentiality of intrinsically-driven TS/TK1-dependent proliferation, introducing a new paradigm in tumor growth with significant therapeutic implications.

Intercellular dTMP transfer supports cancer cell proliferation. To maintain a continuous dTMP supply for DNA replication and proliferation, cancer cells primarily convert deoxyuridine monophosphate (dUMP) to deoxythymidine monophosphate (dTMP, thymidylate) *de novo* by thymidylate synthase (TS, gene name *TYMS*) or salvage extracellular thymidine using thymidine kinase-1 (TK1) (**Fig. 1A**). We used CRISPR/Cas9 to ablate *TYMS* or *TK1* in non-small cell lung cancer (NSCLC) cell lines. TS-KO reduced thymidylate levels, as quantified by mass-spectroscopy (**Extended Fig. 1A-B**), and induced absolute growth arrest but was not lethal. Compared to the parental cells, TS-KO cells were enlarged (**Extended Fig. 1C**) and proliferated only with supplementation of dTMP, but not dUMP **(Extended Fig. 1D)**, an effect observed with different non-overlapping gRNA sequences (**Extended Fig. 1E-F**). Furthermore, when testing different combinations of deoxyribonucleotides, only a combination containing dTTP (deoxythymidine triphosphates) re-established proliferation in TS-KO cells (**Extended Fig. 1G**). On contrary, knockout of *TK1* minimally affected cell growth (**Extended Fig. 2A-B**), implying that proliferation *in vitro* is primarily supported by TS-dependent *de novo* dTMP synthesis. Thereby, TS-KO cells represent a growth-deficient cell model that is entirely dependent on exogenous dTMP for proliferation.

To monitor the proliferation dynamics of dTMP-deficient cells, *TYMS* was knocked out in NSCLC cell lines that express nuclear H2B-GFP, allowing for real-time tracking of GFP^+ TS-KO cells in coculture with unlabeled parental cells (**Fig. 1B**). Unexpectedly, the TS-KO cells displayed restored growth when cocultured with parental cells, whereas TS-KO cells cultured alone failed to proliferate (**Fig. 1C)** and the morphology of cocultured TS-KO cells reverted to normal **(Extended Fig. 2C)**. The findings were confirmed using TS-KO cells

generated by two other non-overlapping gRNAs in two different cell lines, where parental cell-dependent growth of TS-KO cells was replicated **(Extended Fig. 2D**). The quantification of the proliferative capacity of TS-KO cells was however limited by the spatial constraint from proliferative parental cells, and therefore a long-term coculture was established. A coculture of GFP^+ TS-KO A549 cells and parental cells was expanded for 10 passages in sub-confluent conditions and the GFP^+ TS-KO cells were flow-sorted and counted (**Fig. 1D**). When isolated, the sorted TS-KO cells failed to proliferate in absence of dTMP supplementation (**Fig. 1E**), demonstrating the stable nature of the dependency of TS-KO cells on parental cells for proliferation.

Next, to determine whether a similar observation could be made upon deficiency of other dNTPs, *RRM1* (to deplete all dNTPs) and *DTYMK* (to deplete pyrimidines) were knocked out in A549 cells (**Extended Fig. 2E-F)**. The growth defect arising from nucleotide depletion was, however, not restored in the coculture (**Extended Fig. 2G**), indicating the specificity of dTMP as the shared nucleotide between cells. To further demonstrate that dTMP equilibration across the coculture causes the proliferation of TS-KO cells, parental A549 cells were cultured in L-Serine-3-^{13}C (Ser^{13C}) because Serine's C-3 is transferred to dUMP to synthesize dTMP (**Extended Fig. 3A**). Serine by itself did not reinstate the growth of TS-KO cells (**Extended Fig. 3B**). We also tested if nucleotides released by dead parental cells could support TS-KO cells proliferation but did not observe a rescue. (**Extended Fig. 3C-D**). Therefore, parental cells preincubated with Ser^{13} were cocultured with puromycin-resistant TS-KO cells. Once the re-growth of TS-KO cells was detected in coculture, parental cells were eliminated by puromycin treatment and $dNTP^{13C}$ levels were quantified in proliferating TS-KO cells by mass spectrometry (**Fig. 1F**). As a result, dTMP levels were found re-equilibrated to the levels measured in parental cells, along with dTDP and dTTP (thymidine diphosphate and triphosphate respectively) (**Fig. 1G**), indicating that transfer of dTMP from the parental cells can rescue the growth defect caused by perturbation of the *de novo* dTMP synthesis.

To investigate if a collective modality of proliferation for dTMP-low cells exists also in tumors, single cell sequencing data of 40 NSCLC patients were pooled[7] and the gene expression profiles of the various cell types were analyzed (**Extended Fig. 4A**). Interestingly, a significant proportion of the cancer cells lacked expression of *TYMS* (encoding TS) and *TK1* (*$TYMS^-TK1^-$*) in the cancer clusters (**Extended Fig. 4B**). In some patients *$TYMS^-TK1^-$*

comprised of more than 80% of the total cancer cell population (**Extended Fig. 4C**). Notably, when examining cells positive for the proliferation marker *MKI67* (in samples with over 50 proliferative cells) a substantial proportion of *TYMS*$^-$*TK1*$^-$ cells was observed in all samples, reaching 50% of the total *MKI67*$^+$ cells in certain cases (**Fig. 1H**). This highlights the significant contribution of *TYMS*$^-$*TK1*$^-$ cancer cells to tumor growth. Furthermore, *TYMS*$^-$*TK1*$^-$ cells frequently expressed other proliferative genes along with basic metabolic genes (**Extended Fig. 4D**), further validating the non-quiescent nature of this subpopulation. Next, a spatial transcriptomic dataset was analyzed to evaluate the distribution of *TYMS*$^-$*TK1*$^-$ cells in NSCLC tumors. The cells were found to be interspersed with other populations (*TYMS*$^+$*TK1*$^-$, *TYMS*$^-$*TK1*$^+$, *TYMS*$^+$*TK1*$^+$) (**Fig. 1I** and **Extended Fig. 5A**). Interestingly, a neighborhood analysis performed by calculating the proportion of different cell populations in successive radii revealed a remarkable tendency of *TYMS*$^-$*TK1*$^-$ cells to cluster near *TYMS*$^+$*TK1*$^+$ cells (**Fig. 1J**). Meanwhile, these observations were not found in the other groups of *TYMS*$^-$*TK1*$^+$ and *TYMS*$^+$*TK1*$^-$ populations, which appeared randomly located. *TYMS*$^+$*TK1*$^+$ cells showed the opposite trend (**Extended Fig. 5B**). This suggested that *TYMS*$^-$*TK1*$^-$ cells prefer easy access to the dTMP, potentially released into the extracellular space by the *TYMS*$^+$*TK1*$^+$ cells. To test this, we assessed whether conditioned medium from parental cells could restore proliferation in TS-KO cells when added to their growth medium. Surprisingly, however, this treatment was insufficient to re-establish proliferation of TS-KO cells (**Fig. 1K**). Similarly, parental cells seeded on a transwell-membrane, that was impermeable to mammalian cells but allowed sharing of medium with TS-KO cells, failed to restore growth of the TS-KOs (**Fig. 1L**), thereby validating a need for a physical connection between the cells sharing dTMP.

In summary, dTMP-deficient cells may attain proliferation by acquiring dTMP through direct contact with surrounding viable cells. These observations suggest the dispensability of *de novo* pyrimidine synthesis for growth. Importantly, we have identified a **collective mode of proliferation** relayed by intratumoral equilibration of dTMP.

Collective proliferation drives pathophysiological features of cancer.

Having established collective proliferation *in vitro* and in patients, global transcriptomic changes were analyzed by RNA sequencing in A549 to see how TS-KO cells transition from non-proliferative state to collective growth with parental cells. Differentially expressed genes

149 (DEGs) were used to obtain gene signatures distinguishing non-proliferative TS-KO cells
150 and parental controls (**Extended Fig. 6A**). To identify the molecular changes undertaken
151 during transition from non-proliferative to proliferative state, TS-KO were collected from
152 puromycin-treated coculture after growth restoration and compared to TS-KO cells cultured
153 alone (**Extended Fig. 6B**). Finally, to understand the extent to which proliferative TS-KO
154 cells regained the features of control cells, we compared proliferative TS-KO cells to parental
155 controls (**Extended Fig. 6C**). Epithelial-mesenchymal transition (EMT), which is associated
156 with metastasis and chemoresistance in cancer [8], was significantly enriched in non-
157 proliferating TS-KO compared to TS-expressing controls (Extended Fig. 6A, **Extended Fig.**
158 **6D**). However, during transition to replicative state EMT signatures were downregulated in
159 proliferative TS-KO cells compared to TS-KO cells with growth arrest (Extended Fig. 6B),
160 while still maintaining higher EMT compared to parental controls (Extended Fig. 6C).
161 Opposite trend was observed for the oncogenic KRAS signature, which was reduced in TS-
162 KO cells, and was restored as TS-KO cells regained proliferation (Extended Fig. 6A-C). This
163 implies that cells with dTMP deficiency differ significantly from cells that synthesize
164 endogenous dTMP. Then, these signatures were investigated in *TYMS*$^{-}$*TK1*$^{-}$ cells from the
165 single cell transcriptomic data from patients (Extended Fig. 4). As in the proliferative TS-KO
166 cells in coculture, KRAS, EMT signaling, and senescence-associated genes were
167 upregulated in *TYMS*$^{-}$*TK1*$^{-}$ cells whereas pyrimidine metabolism was downregulated (**Fig.**
168 **2A**). We then further explored the role of senescence, which contributes to many cancer
169 phenotypes[9,10]. TS-KO cells were highly positive for the senescence makers β-
170 galactosidase (**Fig. 2B, Extended Fig. 6E**) and p21 (**Extended Fig. 6F**). Based on the
171 trends in the gene signatures from the TS-KO cells (Extended Fig. 6A-B), we speculated
172 that they would at least partially revert senescence to regain proliferation in coculture.
173 Therefore, we employed quantitative-image-based cytometry (QIBC) to quantify p21 protein
174 expression in both TS-KO and control cells in cocultures at single-cell level. However, the
175 mean expression of p21 in proliferative TS-KO cells in coculture remained unchanged
176 compared to the TS-KO cells cultured alone (**Fig. 2C-D, Extended Fig. 6G**). Same
177 observation was made when p21 levels were quantified by western blot (**Extended Fig. 6H**),
178 indicating that cells in coculture could proliferate despite senescence markers, in line with
179 previous observations[11]. RNA sequencing analysis also associated TS-KO cells with an
180 upregulation of inflammatory signatures (Extended Fig. 6D). Since pyrimidine imbalance has

been linked to cGAS-STING pathway, which is responsible for innate immunity response[12], we quantified active cGAS in cytoplasmic micronuclei[13] in dTMP deficient cells and found its activation to be strongly increased in both TS-KO and TS-TK1-KO cells compared to control cells (**Fig. 2E**). Further, protein quantification of phosphorylated STING and its downstream activator TBK-1 showed upregulation in dTMP deficient cell (**Fig. 2F, Extended Fig. 6I-J**). Since STING pathways is triggered by cytosolic DNA[14], we quantified the levels of cytosolic single stranded DNA (ssDNA) in the cells after labelling them with CldU (5-Chloro-2'-deoxyuridine) and found high amount of ssDNA accumulated in TS-KO cells (**Fig. 2G**). Finally, the expression of γH2AX (a DNA-damage marker) was quantified, as nucleotide imbalance mediated cGAS-STING pathway has been previously associated with genome integrity[15]. Higher γH2AX levels were observed in both TS-KO and TS-TK1-KO cells compared to control cells (**Fig. 2H**). However, remarkably, donor parental cells in cocultures also showed significant increase in γH2AX activation in A549 (**Fig. 2I-J, Extended Fig. 6K**) and Calu-1 cells (**Extended Fig. 6L**), implying that dTMP insufficiency in the “donor” or the “acceptor” cells during collective proliferation could be sufficient to induce replicative stress and DNA damage.

Finally, since dTMP depletion is used as an intervention strategy in clinical oncology, we investigated if collective proliferation might render resistance to drugs that target TS. Therefore, we treated A549 cells with sublethal doses of the TS inhibitor 5-flurouracil (5-FU), which abrogated growth without killing. After drug retraction, parental cells were added to 5-FU treated cancer cells and were found to significantly accelerate their growth restoration, indicating that collective proliferation could also contribute to chemoresistance (**Fig. 2K, Extended Fig. 6M**). To conclude, collective proliferation drives several physio-pathological features of cancer by facilitating the proliferation of dTMP-deficient (including chemotherapy-treated) cells without altering their p21 status and by creating a nucleotide deficit that propagates genomic instability within the cancer population (**Fig. 2L**).

Tumor microenvironment (TME) cells contribute to collective proliferation.

Next, we wanted to evaluate the stringency of the pairing of donor and dTMP-deficient cells in collective proliferation. Therefore, we attempted growth rescue of TS-KO A549 cells (of adenocarcinoma origin) with different lung epithelial cell lines (Calu1 of squamous cell carcinoma origin and BEAS-2B of non-cancerous origin). Remarkably, both Calu-1 and

213 BEAS2B rescued the growth of A549 TS-KO cells in coculture (**Figure 3A**). This observation
214 prompted us to extend our investigation to non-epithelial cells previously associated with
215 nucleoside secretion[16-18]. Of these, tissue-resident fibroblasts (**Figure 3B**), cancer-
216 associated fibroblasts (CAFs, **Figure 3C**) and peripheral blood mononuclear cells (PBMCs)
217 (**Figure 3D**), as well as the transformed Jurkat cells of T-cell origin (**Figure 3E**), failed to
218 restore growth of TS-KO cells. However, human umbilical vein endothelial cells (HUVEC)
219 cells and THP-1 monocytes restored proliferation of TS-KO cells (**Figure 3F-G**). Further
220 looking into macrophages polarization states, (**Figure 3H**), M0 and M2 macrophages
221 rescued the growth defect in TS-KO cells, whereas M1 macrophages did not (**Figure 3I**).
222 Considering that protumor M2 macrophages support TS-KO cell growth and that cancer
223 cells polarize macrophages to a M2-like phenotype (tumor-educated macrophages, TEMs)
224 to secrete pyrimidines[19], we administered A549 cell culture medium (CM) to M0
225 macrophages to polarize them to TEMs. CM was then collected from the TEMs and
226 supplemented with fresh cell-culture medium for TS-KO cells**.** While TEMs had a positive
227 effect on TS-KO proliferation when co-cultured (like M2 macrophages), CM from the same
228 TEMs did not facilitate TS-KO cell proliferation (**Extended Fig. 7A-B**), further confirming that
229 dTMP sharing involves non-secretory routes. We then analyzed scRNA-sequencing data
230 from patients and found a positive correlation between endothelial cells and number of
231 *TYMS*$^{-}$*TK1*$^{-}$ cells, but not with M2 macrophages and epithelial cells (**Figure 3J-L, Extended**
232 **Fig. 7C**). We further performed a neighborhood analysis and found an increased propensity
233 for endothelial cells in *TYMS*$^{-}$*TK1*$^{-}$ cells (**Figure 3M, Extended Fig. 7D**). This could imply
234 that different TME donors could be employed in different tissues depending on the proximity
235 and availability. Thereby a non-specific nature of collective proliferation emerges, where
236 dTMP deficient cancer cells can make physical contacts with different types of TME cells to
237 maintain growth.
238
239 **dTMP exchange is mediated through gap junctions**. Having established that physical
240 contact between cells is necessary for collective proliferation, the next step was to
241 investigate the molecular nature of this coupling. RNA sequencing showed that *GJA1* and
242 *GJD3* were upregulated in growth-deficient and proliferative TS-KO cells, compared to
243 parental control cells (**Extended Fig. 8A**). *GJA1* and *GJD3* code for proteins Connexin43
244 (Cx43) and Connexin30.2 (Cx30.2), respectively. Cx43 and Cx30.2 can hexamerize to form

245 gap junctions between cells, which generates a syncytium for intercellular metabolite
246 exchange and may underpin the growth rescue effect[20,21]. Theorizing that TS-KO cells
247 supply dTMP via gap junctions in coculture settings, the possibility that these cells are
248 diffusively coupled was tested by fluorescence recovery after photobleaching (FRAP).
249 Specifically, a monolayer of NSCLC cells was stained with calcein red-orange AM (size
250 comparable to thymidylate), and a single cell randomly selected in a cluster was bleached
251 within its limits. The post-bleaching recovery of fluorescence was recorded in the bleached
252 cell. Results indicated a strong recovery that was blocked in the presence of carbenoxolone
253 (CBX), a pan-gap junction inhibitor (**Fig. 4A, Extended Fig. 8B**). This implied that gap
254 junctions are potential conduit for the diffusion of dTMP between cells. This was
255 demonstrated by treatment of cocultures with CBX, which significantly reduced the growth
256 rescue of the TS-KO cells at a concentration of CBX that had no effect on the proliferation
257 of the parental cells (**Fig. 4B, Extended Fig. 8C-D**). In contrast, inhibition of nanotunnels
258 (that form another mode of intercellular communication) by SMIFH2[22] did not reduce TS-KO
259 cell growth in coculture (**Extended Fig. 8E-F**). To further validate the role of gap-junctions
260 in three-dimensional setting, we generated spheroids containing TS-KO and parental control
261 cells treated with CBX or vehicle control. While TS-KO cells proliferated within spheroids
262 containing parental cells, their growth was inhibited when these cocultures were treated with
263 CBX (**Fig. 4C, Extended Fig. 8G**). Similarly, CBX treatment prevented THP-1 monocytes
264 from restoring TS-KO cell growth (**Fig. 4D**). Together, these data confirm gap junction-
265 mediated cell coupling as the route for dTMP transfer.
266 Since RNA sequencing data identified *GJA1* and *GJD3* as the main candidates for forming
267 connexins, their protein levels were quantified in TS-KO cells. Expression of Cx43 (encoded
268 by GJA1) was significantly increased in dTMP-deficient TS-KO and TS-TK1-KO cells,
269 compared to the parental cells, as confirmed by western blots (**Figure 4E**) and Cx43
270 immunofluorescence staining (**Figure 4F, Extended Fig. 9A**). Further, Cx43 expression was
271 quantified in proliferating TS-KO cells by western blot and was found to be comparable to
272 that in non-proliferating TS-KO cells (**Figure 4G**). Immunofluorescent staining of donor A549
273 cells from coculture with TS-KO showed that the parental cells also increased Cx43
274 expression (**Extended Fig. 9B**). Therefore, Cx43 was postulated to be the key connexin
275 involved in dTMP equilibration. This was further confirmed in computation based
276 autodocking of dTMP to GJA1 protein, which predicted binding of dTMP to open

277 conformation of Cx43 (**Extended Fig. 9C-D**). Consequently, the absence of Cx43-mediated
278 coupling was hypothesized to abolish the proliferation of TS-KO cells in coculture. Therefore,
279 based on *GJA1* mRNA expression (**Figure 9E**), cells with undetectable levels of *GJA1* were
280 identified for further studies. After confirming the lack of Cx43 expression by western blot
281 (**Figure 4H**), NCI-H1299, NCI-H520 and NCI-H838 cells were cocultured with TS-KO cells.
282 While A549, Calu-1, and SK-MES-1 (Cx43 positive cells) restored growth of the TS-KO cells,
283 the cells lacking detectable Cx43 (NCI-H1299, NCI-H530 and NCI-H838) failed (**Figure 4I**).
284 Moreover, while coculture with Cx43 expressing cell lines reverted TS-KO cells to normal
285 morphology, coculture with GJA1-low cells showed TS-KO cells with stressed morphology
286 (**Fig. 4J**). To further validate the role of GJA1, siRNA-mediated knockdown of GJA1 was
287 introduced into TS-KO cells, as well as in A549 and Calu-1 cells that were used as dTMP
288 donors. While GJA1 knockdown did not affect parental cell growth (**Figure S9F-G**), it
289 significantly reduced the growth of TS-KO cells cocultured with A549 or Calu-1 cells (**Figure**
290 **3K**). Altogether, these findings confirm GJA1 as the major channel of dTMP equilibration.
291
292 **Gap junction-dependent *Tyms*$^{-}$*Tk1*$^{-}$ tumor growth *in vivo***. To test whether cells lacking
293 *de novo* and salvage dTMP synthesis can form tumors *in vivo*, we knocked out *TYMS* and
294 *TK1* in A549 cells (**Extended Fig. 10A-B**) and injected them in the flanks of NSG mice.
295 Despite being unable to grow *in vitro* in the absence of parental dTMP donors (**Extended**
296 **Fig. 10C**), TYMS-TK1-KO cells formed tumors in mice (**Figure 5A**). Protein quantification of
297 isolated tumors confirmed the lack of dTMP synthesizing enzymes together with a significant
298 increase in Cx43 (expressed by GJA1) in TS-TK1-KO tumors (**Figure 5B)**. This result
299 prompted generation of a lung cancer mouse model with genetic ablation of *Tyms* and *Tk1*.
300 Therefore, lung-tropic adeno-associated viruses (AAV) carrying gRNAs for humanized
301 *Kras*^{G12D} mutation, *p53*, *Tyms*, and *Tk1* were delivered to C57BL/6 ROSA-LSL-Cas9 mice[23]
302 to obtain the *Kras*^{G12D}*p53*$^{-/-}$*Tyms*$^{-/-}$*Tk1*$^{-/-}$ (KPTT) model (**Figure 5C, Extended Fig. 10D)**.
303 Mice with *Kras*^{G12D}*p53*$^{-/-}$ (KP) derived tumors[24] were used as controls. Similar to the results
304 from NSG mice, we found that tumors could form and grow in mice without Ts and Tk1 (**Fig.**
305 **5D-E**). However, the cells derived from a KPTT tumor failed to grow *in vitro* without dTMP
306 supplementation and displayed a senescent morphological phenotype upon dTMP
307 deprivation (**Fig. 5F**), similar to observations in human cells. These findings indicate that *in*
308 *vivo* their growth depends on an exogenous source of dTMP. Furthermore KPTT-derived

309 cells (that could not grow without dTMP) could form new tumors when injected in the flanks
310 of wild type C57BL/6 mice (**Fig. 5G**). This confirms their tumorigenicity despite the lack of
311 intrinsic dTMP synthesis.
312 Next, to test the involvement of gap junction in the growth of KPTT cells, the cells were
313 cocultured with a syngeneic cell line Ladi 2.1 (derived from a lung tumor of a C57BL/6 mice)
314 in the presence and absence of CBX. Since KPTT tumors express cytoplasmic GFP[23], the
315 fluorescence signal was used as the proliferation readout. KPTT cells grew in coculture with
316 Ladi 2.1 cells but proliferation was significantly reduced in the presence of CBX (**Figure 5H,**
317 **Extended Fig. 10E**), indicating the role the of gap junctions in their growth. To test this
318 further *in vivo*, mice were intubated to generate KP and KPTT tumors, followed by
319 subcutaneous injection of CBX or vehicle control (NaCl) for 8 weeks. Although no difference
320 was observed in the survival of CBX treated KP mice, the drug significantly reduced and
321 delayed the formation of tumors in KPTT mice and increased their mean survival (**Fig. 5I**).
322 Compared to vehicle control, in the CBX treated KPTT group three mice formed tumors
323 comparable to controls and three mice formed small tumors which didn't develop symptoms
324 that would meet the humane endpoint criteria (**Fig. 5J**). The other mice from this group didn't
325 form detectable tumors. H&E staining of mouse lungs showed that CBX-treated KPTT mice
326 developed tumors of comparatively smaller size with visibly intact parenchyma, compared
327 to the larger tumor burden in controls (**Extended Fig. 10F**). Taken together, these results
328 confirm that tumor growth *in vivo* can proceed without active dTMP synthesis, facilitated by
329 gap junction-mediated dTMP acquisition from surrounding tissue.
330 Our data presents a strong rational to revisit the canonical notion that synthesis of dTMP in
331 every single transformed cell drives tumor growth and establish a new paradigm of collective
332 proliferation. In the postulated model proliferation can be maintained by dTMP being
333 synthesized in some cells within a tumor (both of cancer and non-cancer origin) and
334 redistributed to other cancer cells via gap junctions (**Fig. 5K**).
335

336 **Discussion**

337 The crosstalk of tumor entities at multiple levels is fundamental to cancer growth, such that
338 immunotherapeutic abrogation of receptor-driven interaction between cancer cells and
339 immune cells has been one of the major breakthroughs in the clinical intervention of NSCLC
340 and other cancers[25,26]. Metabolic codependency and cross-feeding of metabolites between

TME and cancer cells further adds to this complexity and is equally important for tumor growth[27,28]. By breaking the dogma of the indispensability of cancer-specific dTMP biosynthesis and by identifying dTMP equilibration within tumor as an important growth mechanism, this study advances the concept and postulates a model of collective proliferation.

The concept of collective proliferation repurposes metabolite sharing and resource redistribution as an energy-efficient compensatory mechanism for metabolic vulnerabilities in tumors[29]. In particular, the redistribution of thymidylate within tumors might be a functional rheostat for adapting to metabolic heterogeneity[30], overcoming the challenges of the harsh growth environment[31] and modulating the dynamics of TME[32]. Moreover, since proliferation is a fundamental physiological process, the concept of collective proliferation may have relevance not only in other cancers, but also in embryogenesis, tissues regeneration, and other proliferative diseases (atherosclerosis, idiopathic pulmonary fibrosis, scleroderma, etc.). Therefore, it is pertinent to understand all the aspects of collective proliferation in more extensive and dedicated studies, which includes the central role of dTMP in collective proliferation, origin and characterization of cells that lack dTMP deficiency, interaction of dTMP deficient cells with donor cells, effect on therapy response, and finally how dTMP sharing contributes to the evolving conundrum of pyrimidine metabolism in cancer.

Firstly, our data that dTMP is the only nucleotide shared during collective proliferation are very remarkable. dTMP is distinct as it is the nucleotide moiety exclusive to the dNTP pool, suggesting it might possess characteristics that are not shared by other dNTPs. These unique features might have important roles in genomic instability and DNA repair during xenobiotic stress, as it has previously been shown that thymidine metabolism is an important determinant of telomere length[33].

Further, understanding the origin of dTMP deficient cells during clonal expansion will be a vital addition to proliferation dynamics in tumor growth. The prime question is whether these cells are reminiscent of cells that fail to overcome oncogene-induced senescense[34] or they are more plastic to modulate dTMP synthesis to the external cues.

This study links the lack of dTMP expressing genes with certain key pathological features. However, a detailed characterization of dTMP deficient cells will unravel the biological nature and clinical implications of this association. Of note, it is important to understand the fate of senescent cancer cells that rely on exogenous dTMP supply, as senescence plays a critical

373 role in cancer progression and treatment response[35]. Moreover, the observed connection
374 with cGAS-STING pathway, a cellular detector of cytoplasmic DNA and innate immune
375 response activator, suggests that dTMP availability (and its fluctuations) may influence
376 tumor inflammation.
377 Furthermore, it is important to note that collective proliferation is an interactive process and
378 includes cells from different lineages, requiring a thorough exploration of its dynamic nature.
379 A detailed study is needed to understand the association between dTMP deficiency and
380 activation of connexin proteins, especially in the donor cells, as we observed that dTMP-
381 deficient cells increased the expression of GJA1 in cells that already had detectable levels
382 of GJA1, while failing to induce its expression in other cells where GJA1 was initially
383 undetectable. Therefore, more detailed insight into epigenetic modulation of these
384 interactions is required. In addition, one of the most intriguing observations that calls for
385 further exploration is the induction of DNA damage in donor cells that participate in dTMP
386 equilibration. This could indicate that collective proliferation is a mean by which genomic
387 instability is propagated in tumors and could have different impacts the non-cancerous donor
388 cells (such as monocytes and endothelial cells) depending on the context of their interaction
389 with cancer cells.
390 A major implication of the outcomes of this research relates to therapeutics for NSCLC and
391 other cancers, since targeted metabolic perturbation is central to chemotherapy, including
392 TS targeting drugs like 5-flurouracil and pemetrexed[36]. In this context, metabolic
393 redistribution by refractory cells might represent a so far overlooked mechanisms of
394 chemoresistance to anti-dTMP-based drugs such as 5-flurouracil and pemetrexed[37,38].
395 Collective proliferation could also contribute to resistance against immune therapy where
396 dTMP deficient cells act as nucleotide sponges that affect the differentiation and exhaustion
397 of immune cells[39]. Subsequently, the model may refine therapeutic avenues, for instance by
398 repurposing CBX, which is approved for peptic, esophageal, and oral ulceration[40], or other
399 gap junction inhibitors, for clinical testing of combination therapies.
400 Finally, collective proliferation, particularly in the context of dTMP equilibration, adds another
401 dimension to the evolving complexity of pyrimidine metabolism in cancer. Recent advances
402 have attributed moonlighting functions to classical metabolites[41,42]. This also includes
403 pyrimidine metabolites that can play a critical role in differentiation[43-47], act as a cofactor in
404 lipogenesis[48], and intercellularly feed glycolysis under metabolic stress[49-51] beyond their role

in DNA synthesis and proliferation. The concept of dTMP sharing in context of collective proliferation highlights the importance of pyrimidine metabolism beyond the terminal outcome of metabolic alterations in cancer to support cell proliferation. Therefore, its critical and diverse roles in survival and growth necessitate studies to identify the cell intrinsic and extrinsic cues that direct pyrimidine metabolites to feed into other essential pathways, compensate for intercellular nutritional stress, or support proliferation of adjacent cells that lack dTMP synthesis.

In conclusion, this study repositions proliferation in the context of metabolic resource sharing and establishes a more dynamic and plastic nature of tumor growth. Further exploration of this mechanism will not only enhance the current understanding of the interplay among tumor growth, heterogeneity, and pathology but will also provide a new perspective to target proliferation.

Acknowledgements. The authors wish to acknowledge the support of Metabolomics Core Facility, EMBL, Heidelberg, Germany for their support with mass-spectrometric quantification, and Dr Thomas Solomon at Blazon Scientific for assistance with drafting the manuscript. The study was funded by Hallas-Møller Ascending Investigator Grant from Novo Nordisk Foundation (PC), Independent Research Fund Denmark 0134-00012B (PC), Lundbeck Foundation, Denmark, R380-2021-1264 (MAS), International Association for the Study of Lung Cancer (MAS), Danish Cancer Society (AMAR), Danish Cancer Society (AMT). Illustrations were drawn using Biorender.

Author Contribution. P.C., M.A.S. and A.M.A.R were involved in project conceptualization and development and the preparation of the manuscript. P.C. was involved in supervision. M.A.S., A.M.A.R., L.P., S.V., S.S.M., P.N.G. A.M.T. and L.B.G conducted the experiments. V.R. and N.P.P. conducted the bioinformatic analysis. L.C.B and M.Ve. performed molecular modeling simulation. S.K., F.N., M.Vo and P.S. were involved in data acquisition.

Declaration of Interests: Authors declare no competing interests.

435 **Materials availability.** All the plasmids generated in this study are available from the lead
436 contact without restriction or with a completed materials transfer agreement, whichever
437 applies.
438
439 **Data and code availability**. RNA sequencing data has been deposited to GEO dataset
440 (GSE271721). Any additional information required to reanalyze the data reported in this
441 paper is available from the lead contact upon request.
442
443 **Methods**
444 **Cell lines**. Lung cancer cell lines (A549, Calu-1, SK-MES-1, NCI-H1299, NCI-520, NC-
445 H838) and THP-1 monocytes were purchased from ATCC. Normal fibroblasts and Cancer
446 Associated Fibroblasts were provided by Dr. Pamela L. Strissel, at the University Clinic,
447 Erlangen, Germany. Ladi 2.1 cells were obtained from Dr. Markus E. Diefenbacher,
448 Biochemistry and Molecular Biology Biocenter, University of Würzburg, Germany. HUVEC
449 cells were provided by Professor Ditte Caroline Andersen, Research Unit for Clinical
450 Biochemistry, Odense University Hospital, Denmark. HEK-293T cells were obtained from
451 Dr. Heiko Wurdak, Faculty of Medicine and Health, School of Medicine, University of Leeds,
452 UK. The KPTT cell line was established from C57BL/6 mouse with genetic knock of Tyms
453 and Tk1. All cells were cultured in DMEM supplemented with 2 mM of L-glutamine (Gibco),
454 100 U/ml of Penicillin–Streptomycin (Gibco), and 10% Fetal bovine serum (Gibco), except
455 for THP-1 and Jurkat cells that were cultured in RPMI 1640 (Gibco) supplemented with 10%
456 FBS (Merch) and 1% penicillin-streptomycin (Gibco). HUVEC cells were cultured in
457 Endothelial Cell Growth Medium 2 medium (PromoCell) supplemented with the ready-made
458 Supplement Mix. All cell lines were authenticated by STR profiling and tested regularly for
459 mycoplasma contamination, kept in culture for no more than 20 passages and maintained
460 at 37°C with 5% CO_2 level in a humidified incubator.

461 **Lentiviral transduction.** To produce lentiviral particles, HEK 293T cells were transfected
462 with 8 µg expression vectors and 2 µg of third-generation lentiviral packaging system in
463 complex with 24µg PEI (Polysciences) in 1.2 ml of 0.9% NaCl. After 48 hours, the
464 supernatant containing the lentiviral particles carrying the gRNAs was collected, centrifuged,
465 and filtered. For transduction, 50,000 cells were seeded in a 6-well plate and transduced
466 with lentiviral vectors carrying transgenes in presence 32 µg polybrene (Sigma). Viruses

467 were removed 24 hours post the transduction, and selection was started 48 hours post
468 transductions. TS-KO cells and TS-TK1-KO cells were selected with 3 μg/ml puromycin
469 (Sigma). Cells transfected with gRNA for TK1, DTYMK, and RRM1 were selected with 1 mg
470 /ml hygromycin (Sigma). H2B-GFP or H2B-RFP transduced cells were flow-sorted for green
471 and red positivity respectively. Plasmids and gRNA sequences are listed as Extended Table.
472
473 **Incucyte real-time Proliferation Assay.** For Incucyte real-time proliferation assay, cells
474 were seeded in 96-well plates at a density of 1,800 – 2,000cells/well. For cocultures 1,800 -
475 2,000 TS-KO or TS-TK-KO cells were seeded with donor cells in ratios mentioned in the
476 respective figure legends. Plates were scanned at regular intervals of 4 hours – 24 hours
477 using basic analyzer module. Incucyte 2021C software was used for analysis. In brief, 8 –
478 10 images were used to train the software to differentiate cells from background to calculate
479 confluency as the area of the plate occupied by cells. Similarly, Top Hat background
480 subtraction method was applied to the fluorescent signals to define nuclei. Processing
481 definition was created from the training set that was applied to all scans and proliferation
482 kinetics were created as proliferation over time and number of nuclei over time.
483
484 **Metabolite treatments.** For metabolite treatments, H2B-GFP^{+} TS-KO cells were seeded at
485 a density of 1800–2000 cells/well in a 96-well plate. Medium was changed on the following
486 day and cells were then treated with metabolites as indicated in the figure legends. Plates
487 were scanned and analyzed using Incucyte real-time proliferation assay. Thymidylate
488 (dTMP), thymidine (Thd), deoxyuridine monophosphate (dUMP), and deoxythymidine
489 triphosphate (dTMP) were purchased at Sigma. Deoxyadenosine triphosphate (dATP),
490 deoxyguanosine triphosphate (dGTP), and deoxycytidine triphosphate (dCTP) were
491 purchased at Promega.
492
493 **THP-1 differentiation.** THP-1 monocytes were differentiated into macrophages by
494 stimulation with phorbol 12-myristate 13-acetate (PMA). Briefly, 800,000 THP-1 cells were
495 stimulated with 100 ng/ml PMA for two days in a 6-well plate. During the stimulation, the
496 THP-1 cells would adhere to the surface of the well. To further differentiate the macrophages
497 into M1- or M2 macrophages, the cells were stimulated with 100 ng/ml lipopolysaccharide
498 (LPS) (Sigma-Aldrich) and 20 ng/ml interferon gamma (IFNγ) (Peprotech) or 20 ng/ml

499 interleukin 4 (IL4) (Peprotech) respectively for 72 hours. During the M1- and M2 polarization,
500 M0 macrophages were cultured in RPMI supplemented with 10% FBS and 1% penicillin-
501 streptomycin.
502
503 **PBMC isolation.** Peripheral blood mononuclear cells (PBMCs) were isolated from healthy
504 individuals using Lymphoprep separation (StemCell Technologies) according to the
505 manufacturer's instructions. Isolated PBMCs were frozen in FBS with 10% DMSO. Prior to
506 use in co-culture experiments, PBMCs were thawed and seeded in X-vivo medium (Lonza)
507 supplemented with 5% human serum (Sigma) at a density of 1.5 x 10^6 cells/well in a 24-well
508 plate. The cells were rested for overnight in a 37°C, 5% CO2 incubator. To ensure an
509 enrichment of T cells, cells were then collected from the 24-well plate by resuspension,
510 eliminating cells that had adhered to the bottom of the well overnight.
511
512 **Coculture experiments.** For coculture experiments, 1,800–2,000 H2B-GFP-TS-KO (or TS-
513 TK1-KO cells) cells were seeded with dTMP donor cells in 96-well plates. Coculture was
514 optimized by trying different ratios between TS-KO and the dTMP donor cells. For coculture
515 with A549, Calu-1, SK-MES-1, BEAS-2B, NCI-H1299, NCI-H838, and NCI-520 a ratio of 1:4
516 was used. Jurkat cells were stimulated with CD3/CD28 dynabeads (Gibco) according to the
517 manufacture's protocol (Gibco) during the duration of the coculture. HUVEC cells were
518 cocultured with TS-KO cells in presence of combined medium (25% DMEM: 75% HUVEC
519 medium). The proliferation of the H2B-expressing cells was monitored using Incucyte S3.
520
521 **Tumor-educated macrophages.** Tumor-educated macrophages (TEM) were generated as
522 described previously[19]. Initially, 1.5 million A549 cells were cultured in DMEM supplemented
523 with 10% FBS, 1% P/S, and 1% L-glutamine in a 10-cm dish. One day after seeding, the
524 medium was changed on the 50% confluent A549 cells, and the cells were cultured for an
525 additional 48 hours. Next, the conditioned medium was collected from the A549 cells and
526 centrifuged at 300 × g for 5 minutes. The conditioned medium was then filtered through a
527 0.45 um filter and heat-inactivated for 15 minutes at 100°C. DMEM supplemented with 10%
528 FBS, 1% P/S, and 1% L-glutamine was added to the conditioned medium to restore the
529 initial volume. Like the *THP-1 differentiation* described above, 1.6 million THP-1 cells per
530 well of a 6-well plate were stimulated with 100 ng/ml PMA for 48 hours. Then the medium

531 was removed and replaced with 75% heat-inactivated conditioned medium from the A549
532 cells. The THP-1 cells were cultured for an additional 48 hours to polarize them into TEM.
533 Then the conditioned medium from the TEMs was collected, centrifuged at 300 × g for 5
534 minutes, and heat-inactivated at 100°C for 15 minutes. Condition medium was added to was
535 added to 1,800 A549 GFP^+ TS-KO cells in three different ratios (1:4, 1:1 and 4:1) in a 96-
536 well plate. The TEM macrophages were trypsinized and cocultured with KO cells.
537 Proliferation was monitored using Incucyte S3 real-time proliferation assay.
538
539 **Transwell cocultures**. 0.4 µm pore polyester membrane transwells (Corning) were used
540 for transwell cocultures. 2,000 A549 cells were seeded on the upper chamber and the 8000
541 GFP^+ TS-KO cells were seeded on the lower chamber. The growth of TS-KO cells was
542 monitored by Incucyte S3 to obtain the proliferation kinetics.
543
544 **Drug treatments.** Carbenoxolone (CBX, Sigma) and SMIFH2 (Tocris) were first titrated in
545 cells to determine the non-toxic concentrations. For cocultures, 60,000 parental cells and
546 TS-KO cells were seeded per well in a 12 well plate in the determined concentration of the
547 drugs (100 µM CBX and 50 µM SMIFH2), along with the respective vehicle controls (0.1 %
548 NaCl for CBX, 0.1 %DMSO for SMIFH2). One day after the treatment, cells were trypsinized,
549 counted and coculture was set-up as described in previous section. During the coculture
550 cells were maintained in treatment conditions and proliferation was monitored using Incucyte
551 real-time proliferation assay.
552
553 **Spheroid coculture.** 2,000 TS-KO cells per well were seeded in the presence or absence
554 of parental cells treated with 100 µM CBX or 0.1 % NaCl in a 96-well ultra-low attachment
555 plate. The plate was centrifuged at 300 rpm for 10 minutes at 20°C and then incubated at
556 37°C for three days until the spheroids attained a desired diameter of 200–500 µm. The
557 spheroids were then re-treated with CBX (100 µM) or with 0.1% NaCl. Next, the plate was
558 pre-cooled on ice, Matrigel matrix (Corning) was added to the spheroids, and the plate was
559 centrifuged at 300 rpm for 5 minutes at 4°C. Then, the matrigel was polymerized in an
560 incubator at 37°C for 30 minutes. The brightfield and green area of the spheroids were
561 measured using a real-time spheroid invasion assay every 4 hours in Incucyte S3.
562

563 **Western blot.** For western blots, 5–20 µg of protein were resolved on 12% bis-acrylamide
564 gel and transferred on 0.45 µm PVDF membrane (Thermo). Membranes were blocked in
565 5% milk (Biorad) or 3% BSA (Sigma), both prepared in 1X TBS-T (1% Tween20 in Tris Buffer
566 Saline). Membranes were then incubated with primary antibody (diluted in the respective
567 blocking buffer) overnight at 4°C. Post incubation, membranes were washed with 1X TBS-
568 T and incubated with HRP-conjugated secondary antibody for an hour at room temperature.
569 After washing again with 1X TBS-T, ECL substrate (Thermo) was applied to the membrane
570 and the bands were recorded on X-RAY films (Thermo) and developed and fixed manually.
571 A list of antibodies and dilutions is provided in Extended Table 2.
572
573 **β-Galactosidase staining**. A Senescence β-Galactosidase Staining Kit (Cell Signaling
574 Technology) was used. In brief, cells were seeded at low confluence in a 6- or 12-well plate.
575 24 hours post seeding, the medium was changed, and the cells fixed and stained following
576 the instructions from the manufacturer. Stained cells were visualized and imaged using an
577 Olympus BX53 microscope. Positive cells and total cells were counted using ImageJ and
578 positively stained cells were normalized to the total number of cells.
579
580 **siRNA transfection**. Reverse transfection was done with Lipofectamine RNAiMAX
581 Transfection Reagent (Thermo). The transfection complex was prepared by adding 80 nM
582 siRNA to 2 µl transfection reagent in 200 µl serum free DMEM and incubated for 15 minutes.
583 After incubation, the transfection complex was added to the bottom of 12-well plates, and
584 60,000 suspended in 800 µl and added to the wells on top of the transfection complex. Cells
585 were incubated at 37°C in 5% CO_2. 24 hours post transfection, cells were used to establish
586 cocultures. Knock down was confirmed in the lysates that were collected 48 hours post
587 transfection.
588
589 **Immunofluorescence.** For immunofluorescence, 100,000 cells/well were seeded in 6-well
590 plates on coverslips (VWR). For coculture conditions, H2B-fluorescent tagged TS-KO cells
591 were seeded with untagged parental cells. One day post seeding, cells were fixed with 4%
592 formaldehyde (VWR) for 5 minutes followed by 10 minutes of permeabilization with 1X PBS-
593 T (0.1% Triton-X100 in 1X PBS). Cells were blocked in 3% blocking buffer (3% BSA in PBS-
594 T) and incubated in primary antibody (diluted in blocking buffer) overnight at 4°C. Then, cells

595 were washed with 1X-PBS and incubated with secondary anti-rabbit antibody conjugated
596 with Alexa-488 or Alexa (diluted in blocking buffer) for an hour. Cells were then mounted in
597 DAPI containing mounting medium and visualized using an Olympus BX53 microscope.
598
599 **FRAP for measuring coupling.** Monolayers in 4-well ibidi imaging slides were loaded with
600 calcein red-orange (Invitrogen, F10319) for 10 minutes in HEPES RPMI (Thermo). Medium
601 was then replaced by fresh medium to remove unloaded dye. Confluent monolayers were
602 imaged using a Zeiss LSM 700 confocal microscope. A cell in the middle of a confluent
603 cluster was selected for bleaching (high-power 555 nm) until fluorescence at 555 nm
604 excitation and emission >590 nm decreased by 50%. The fluorescence signal was
605 measured in the central cell, neighboring cells, and more remote cells, and normalized to
606 the initial intensity. Recovery was fitted to a monoexponential to calculate calcein
607 permeability (in μm/minutes) from the product of the geometric perimeter and the area of
608 the central cell, divided by the time constant of fluorescence recovery. Permeability from
609 FRAP recording was calculated as described previously (*10*).
610
611 ***In vitro* quantification of C^{13} thymidylate.** For $dTMP^{13}$ quantification in TS-KO cells, A549
612 parental cells (puromycin sensitive) were seeded at a density of 2 million cells in a 10-cm
613 culture dish. After 24 hours, medium was replaced with medium supplemented with 400 μM
614 1-^{13}C-Serine (Sigma). 24 hours post C^{13} enrichment, 1 x 10^6 A549 H2B-GFP TS-KO cells
615 were seeded with C13 enriched parental cells. Cell growth was monitored using Incucyte
616 S3. When the growth of the TS-KO cells was restored, 10 μg/ml puromycin was added to
617 the culture to eliminate the puromycin sensitive parental cells. Following clearing of the
618 parental cells form the culture, TS-KO cells were washed five times with 1X PBS and then
619 1 ml of prechilled extraction solution was added (Methol:Isonitrile:Water; 2:2:1). Cells were
620 incubated on dry ice for 20 minutes and then scraped and collected in 2 ml Eppendorf tubes.
621 After further homogenization on dry ice via a bead beater (FastPrep-24; MP Biomedicals,
622 CA, USA) at 6.0 m/s (3 x 30 seconds, 5 minutes pause time) using 1.0 mm zirconia/glass
623 beads (Biospec Products), samples were centrifuged at 15,000 × g, 4°C for 10 minutes using
624 a 5415R microcentrifuge (Eppendorf) and supernatants were transferred. The remaining
625 pellet was reextracted by addition of 500 μL of a mixture of H_2O:MeOH:ACN (1:2:2, v/v) and
626 bead beating (see conditions described above). After centrifugation, supernatants of

627 corresponding samples were combined and dried under a stream of nitrogen (Organomation
628 Microvap). Dried samples were reconstituted in 50 µL H_2O:MeOH:ACN (1:2:2, v/v),
629 vortexed, centrifuged, and transferred to an analytical glass vials. The LC-MS/MS analysis
630 was initiated within one hour after the completion of the sample preparation.
631
632 **LC-MS/MS analysis**. LC-MS/MS analysis was performed on a Vanquish UHPLC system
633 coupled to an Orbitrap Exploris 240 high-resolution mass spectrometer (Thermo) in positive
634 ESI (electrospray ionization) mode. Chromatographic separation was carried out on an
635 Atlantis Premier BEH Z-HILIC column (Waters; 2.1 mm x 100 mm, 1.7 µm) at a flow rate of
636 0.25 mL/minutes. The mobile phase consisted of water:acetonitrile (9:1, v/v; mobile phase
637 phase A) and acetonitrile:water (9:1, v/v; mobile phase B), which were modified with a total
638 buffer concentration of 10 mM ammonium acetate. The aqueous portion of each mobile
639 phase was adjusted to pH 9.0 via addition of acetic acid. The following gradient (20 minutes
640 total run time including re-equilibration) was applied (time [minutes]/%B): 0/95, 2/95,
641 14.5/60, 16/60, 16.5/95, 20/95. Column temperature was maintained at 40°C, the
642 autosampler was set to 4°C, and the sample injection volume was set to 5 µL. dTMP
643 isotopologues were recorded via a targeted selected ion monitoring (tSIM) scan with a mass
644 resolving power of 120,000 over a 5 Da isolation window set to m/z = 322.5 (scan time: 150
645 ms, RF lens: 70%). Ion source parameters were set to the following values: spray voltage: -
646 3500 V, sheath gas: 30 psi, auxiliary gas: 5 psi, sweep gas: 0 psi, ion transfer tube
647 temperature: 350°C, vaporizer temperature: 300°C.
648 All experimental samples were measured in a randomized manner. Pooled quality control
649 (QC) samples were prepared by mixing equal aliquots from each processed sample. Multiple
650 QCs were injected at the beginning of the analysis to equilibrate the analytical system. A QC
651 sample was analyzed after every 5th experimental sample to monitor instrument
652 performance throughout the sequence. For determination of background signals and
653 subsequent background subtraction, an additional processed blank sample was recorded.
654 Data was processed using TraceFinder 5.1 and raw peak area data was exported for relative
655 metabolite quantification.
656
657 **Cell-line derived xenografts.** For cell line derived xenografts, 500,000 cells were
658 suspended in 40 µl Matrigel (Corning)/1X PBS (1:1). Cells were subcutaneously injected in

659 the flanks of 8–12 week-old female NSG (NOD scid gamma, Charles Rivers Laboratories)
660 mice. Once palpable tumors were observed, mice were sacrificed, by cervical dislocation
661 and tumors were excised and weighed. Tumor volumes were calculated from length and
662 breadth of tumors obtained from caliper measurements using the formula $\pi/6 \times \text{length}^2 \times$
663 width. Mouse experiments were approved by The Danish Animal Experiments Inspectorate
664 at Dyreforsoegstilsynet (License Number 2020-15-0201-00691) and all ethical
665 considerations were followed. Number of mice have been specified for each experiment in
666 their respective figure legends.
667
668 **CRISPR/Cas9-mediated lung tumorigenesis**. Ultra-purified recombinant adeno-
669 associated viral particles carrying gRNA for *Kras-p53* (AAV-KP) and *Kras-p53-Tyms-Tk1*
670 (KPTT) were produced and obtained from VectorBuilder Inc., USA. For experiments
671 B6J.129(B6N)-Gt(ROSA)$^{26Sortm1(CAG\text{-}cas9*,\text{-}EGFP)Fezh/J}$ mice were used which expressed Cas9
672 controlled by lox-Cre-lox (LSL) inducible site. Mice (8–40 weeks) were randomized for age
673 and gender and a viral titer of 3×10^{11} was delivered via an oropharyngeal route to the lungs
674 of C57BL/6 mice with cre-controlled expression of Cas9 (B6J.129(B6N)-
675 Gt(ROSA)$^{26Sortm1(CAG\text{-}cas9*,\text{-}EGFP)Fezh/J}$), resulting in two mouse genotypes:
676 B/6.Kras$^{G12D/G12D}$p53$^{\Delta/\Delta}$ (KP) and B/6.Kras$^{G12D/G12D}$p53$^{\Delta/\Delta}$Ts$^{\Delta/\Delta}$Tk1$^{\Delta/\Delta}$ (KPTT). Mice were
677 weighed weekly and sacrificed when they reached the humane endpoint defined by
678 asphyxiation, 20% drop in body weight and immobility. Lungs were then collected and fixed
679 in 4% buffered formalin and stained for H&E. For CBX treatment, KP and KPTT mice were
680 subjected to biweekly treatment of 40 mg/kg CBX or corresponding volume of 0.9% NaCl
681 (vehicle control). Mouse experiments were approved by The Danish Animal Experiments
682 Inspectorate at Dyreforsoegstilsynet. License Number 2020-15-0201-00607. All ethical
683 consideration were followed.
684
685 **Flow cytometry and sorting.** For FACS of A549 H2B-GFP TS-KO cells in coculture, cells
686 were trypsinized and resuspended in PBS. GFP$^+$ TS-KO cells were gated using a non-GFP
687 parental control. Sorted TS-KO and parental cells were reseeded for cocultures and
688 monitored in Incucyte S3 for proliferation. For counting GFP$^+$ KPTT cells, cells were
689 trypsinized, resuspended in PBS, and run on a FACS Aria-III flow cytometer (BD). GFP+
690 cells were gated on the FITC channel. Data was analyzed on FlowJo.

691

692

693 **Quantitative-image-based cytometry (QIBC)**

694 For QIBC analysis a coculture was set up in 6 well plates on coverslips (12,000 TS-KO cells
695 and 4000 parental cells, TS-KO cells were tagged either with H2B-GFP or H2B-RFP).
696 Proliferation was monitored in Incucyte S3 and when growth was observed in TS-KO cells
697 in coculture, cells were fixed with 4% formaldehyde buffered with 0.5–1.5% methanol (VWR,
698 9713) for 12 minutes at room temperature, washed with ice-cold 1X PBS and permeabilized
699 with 0.1% Triton-X in PBS. For CldU treatment, cells were incubated with 10 μM of CldU for
700 48 hours before co-culture for another 2-3, fixed and permeabilized as outlined above. All
701 antibodies were diluted in Dulbecco's modified Eagle's medium (DMEM, high glucose,
702 Glutamax) containing 10 % FBS. Coverslips were then incubated with primary antibodies
703 for 1 h in dark at room temperature and washed with three times each with 1X PBS and then
704 Coverslips were washed with PBS containing 0.2 % Tween (Sigma-Aldrich). Primary
705 antibodies with the dilutions used were: p21 (1:500 rabbit), p-TBK1 (1:500, rabbit), and
706 γH2AX (1:2,000, mouse, Biolegend, 613402). Next, secondary antibody conjugates of Alexa
707 Fluor 488 or 568 for mouse (A-11029 or A-11031) and rabbit (A-11034 or A-11036)
708 (ThermoFisher Scientific) in 1:2,000 dilutions were used. Secondary-antibody incubations
709 were performed at room temperature for 30 minutes and were supplemented with 4′,6-
710 diamidino-2-phenylindole dihydrochloride (DAPI, 0.5 μg/ml) to counter-stain DNA. After
711 three washes in PBS, coverslips were washed twice in distilled water, dried and mounted in
712 4.5 μl Mowiol-based mounting medium (containing Mowiol 488 (Calbiochem)/glycerol/Tris-
713 HCL, pH 8.5). For QIBC, images were acquired with a ScanR inverted microscope high-
714 content screening station (Olympus) equipped with wide-field optics, air objective, fast
715 excitation and emission filter-wheel devices for DAPI, FITC, Cy3, and Cy5 wavelengths, an
716 MT20 illumination system, and a digital monochrome Hamamatsu ORCA-Flash 4.0LT CCD
717 camera. Images were acquired in an automated fashion with the ScanR acquisition software
718 (Olympus, 3.4.1). In total, 81–144 images were acquired containing at least 1,000 cells per
719 condition. Acquisition times for the different channels were adjusted for non-saturated
720 conditions in 12-bit dynamic range, and identical settings were applied to all the samples
721 within one experiment. Images were processed and analyzed with ScanR analysis software.
722 First, a dynamic background correction was applied to all images. The DAPI signal was then

723 used for the generation of an intensity-threshold-based mask to identify individual nuclei as
724 main objects. This mask was then applied to analyze pixel intensities in different channels
725 for each individual nucleus. For analysis of sub-nuclear foci, additional masks were
726 generated by segmentation of the respective images into individual spots with intensity-
727 based or spot-detector modules included in the software. Each focus was defined as a sub-
728 object, and this mask was used to quantify pixel intensities in foci. After this segmentation
729 of objects and sub-objects, the desired parameters for the different nuclei or foci were
730 quantified, with single parameters (mean and total intensities, area, foci count, and foci
731 intensities) as well as calculated parameters (sum of foci intensity per nucleus). These
732 values were then exported and analyzed with TIBCO Spotfire Software, version 12.2, to
733 quantify absolute, median, and average values in cell populations and to generate all color-
734 coded scatter plots. Within one experiment, similar cell numbers were compared for the
735 different conditions (at least 1000 cells), and for visualization low x-axis jittering was applied
736 (random displacement of objects along the x axis) to make overlapping markers visible.
737
738 **RNA-sequencing.** Total RNA was isolated as per the manufacturer's protocol (Qiazol) from
739 A549 parental cells, A549 TS-KO and coculture conditions. Similarly, total RNA was isolated
740 from lung tumor tissues of KP and KPTT mice (tumors were stored in RNase later and
741 processed simultaneously). 500 ng of total RNA was diluted in 25 µl of nuclease-free water
742 to construct the sequencing libraries using a NEBNext Ultra RNA Library Prep Kit for Illumina
743 followed by paired-end sequencing using a NovaSeq 6000 platform (Illumina), as described
744 by the manufacturer's protocol. Fastq files generated from the sequencing were subjected
745 to quality control analysis using the FastQC package. Alignment of the reads to the human
746 reference genome (GRCh38 release 105) along with the respective human gene annotation
747 file was performed using STAR aligner v2.7.9a. The GRCm39 release 108 was used as the
748 reference genome for the mouse genome alignment. After the alignment, the reads were
749 counted using the Feature counts function in the Rsubread v2.10.5 package in R 4.2.1 and
750 subjected to differential gene expression analysis using the DESeq2 v1.36.0 package in R
751 with an adjusted p-value<0.001 and a fold change of 2.
752
753 **Single-cell RNA-sequencing.** Single-cell RNA-sequencing data of tumors from lung cancer
754 patients were obtained from the public repository Gene Expression Omnibus (GSE148071,

755 N = 42). The analysis was performed as described previously (*18*). In brief, the obtained raw
756 data was subjected for quality control analysis and cells with a number of genes expressed
757 < 200 & > 5000, UMIs with > 30,000 number of molecules, and > 30% of mitochondrial
758 content were removed. The filtering of cells was performed for each patient's sample and
759 also in a pooled manner. Two patient samples (patient 19 and patient 27) were excluded
760 from the analysis as the raw data contained duplicate gene names. Seurat v4.2.1 was used
761 to normalize the counts for the library size and identified 600 variable genes to scale the
762 data for the principal component analysis (PCA). Cell clusters were identified with the first
763 20 principal components from PCA and using a Lovain algorithm with a resolution set to 1.0.
764 The identified cell clusters were visualized using uniform manifold approximation and the
765 projection (UMAP) dimensionality reduction method. Cell clusters were scored and assigned
766 to one of 11 major cell types based on the manual inspection of the cell type markers'
767 normalized expression level in UMAP, and also with the differentially expressed genes level
768 using the FindAllMarkers function in Seurat. The highest scored cell type was assigned to
769 each cluster. Markers used for the cell type assignment were: Endothelial cells (*CLDN5*,
770 *VWF* and *PECAM1*), fibroblasts (*COL1A1*, *COL1A2* and *DCN*), neutrophils (*CSF3R*,
771 *S100A8* and *S100A9*), mast cells (*GATA2*, *TPSAB1* and *TPSB2*), alveolar cells (*CLDN18*,
772 *AQP4* and *FOLR1*), T cells (*CD2*, *CD3D*, *CD3E* and *CD3G*), epithelial cells (*CAPS* and
773 *SNTN*), myeloid cells (*CD14* and *LYZ*), B cells (*CD79A* and *CD79B*), and follicular dendritic
774 cells (*FDCSP*).
775 Cancer cell clusters were assigned as *EPCAM*-positive cells that was also negative for
776 normal lung epithelial makers. In four patient samples, we did not find cancer cell clusters
777 (patient 7, patient 11, patient 37 and patient 42). In the subsequent analysis, cell clusters
778 assigned with the same cell type were pooled together. The number of cells in each cell type
779 per patient is provided in the Supplementary Data S1. Next, cancer cell clusters were filtered
780 to categorize each cancer cell based on *TYMS* and *TK1* expression levels. In brief, cells
781 were assigned as follows: normalized expressions of *TYMS* > 0 and *TK1* = 0 as $TYMS^{+}TK1^{-}$
782 , *TYMS* = 0 and *TK1* > 0 as $TYMS^{-}TK1^{+}$, *TYMS* > 0 and *TK1* > 0 as $TYMS^{+}TK1^{+}$, and finally
783 *TYMS* = 0 and *TK1* = 0 as $TYMS^{-}TK1^{-}$. The number of cells in each of the categorized cell
784 sub-types based on *TYMS* and *TK1* expression for each patient is provided in
785 Supplementary Data S2.

With the assigned *TYMS* and *TK1* expression status for the cancer clusters, gene set enrichment analysis (GSEA) was performed utilizing the hallmark gene sets and other gene sets related to senescence and pyrimidine metabolism collected from MSigDB v2023.2.Hs and gene sets for chromosomal instability and immune response from previous reports (*44-46*). The details of the gene sets are provided in the Supplementary Data S3. A ranked gene list based on a log2 fold change was generated using FindMarkers function by comparing the $TYMS^{-}TK1^{-}$ to the rest of the cancer cell types ($TYMS^{+}TK1^{-}$, $TYMS^{-}TK1^{+}$ and $TYMS^{+}TK1^{+}$). GSEA was performed using fgsea package in R for the rank ordered gene list with the obtained gene sets in each patient sample. Significant gene sets were filtered with a p-value < 0.05 and the number of occurrences of each gene set across patient samples (N = 36) were tabulated. With a threshold of more than 10 patient samples, the gene sets were considered to be either enriched or diminished in $TYMS^{-}TK1^{-}$ cells compared to the other cell states ($TYMS^{+}TK1^{-}$, $TYMS^{-}TK1^{+}$ and $TYMS^{+}TK1^{+}$). A detailed list of enriched gene sets in each patient sample is provided in Supplementary Data S4. In case of proliferative marker analysis, cancer cells positive for *MKI67* marker (*MKI67* > 0) were filtered and analyzed for the proportion of different cell states based on *TYMS* and *TK1* expression levels. The number of each cell subtype status in the *MKI67* subset population is listed in Supplementary Data S5.

Autodocking of GJA1 with dTMP

The structures of the Cx43 receptor in a fully closed state with the N-terminal gate closed (GCN) and a fully open state with the N-terminal lining the pore (PLN) were obtained from the Protein Data Bank with PDB IDs 7F94 and 7XQJ, respectively[52]. Missing loops were built by homology modeling using the Swiss Model server[53]. The ligand, thymidine-5'-phosphate, was obtained from the PubChem database[54]. Its protonation state was calculated using MarvinSketch. Both the ligand and receptor structures were imported into the Molegro Virtual Docker suite for molecular docking studies[55]. For the ligand, charges were assigned according to its protonation state, and all rotatable bonds were set as free. In both GCN and PLN conformations, blind docking was initially performed, followed by target docking. The Simplex Evolution algorithm and MolDock Score were used as the search algorithm and scoring function, respectively. Finally, the results were analyzed using the PLIP server[56], and intermolecular interactions were visualized using PyMol[57].

Neighborhood analysis of Visium spatial sequencing. Spatial data was downloaded from X10 genomics (https://www.10xgenomics.com/datasets/human-lung-cancer-ffpe-2-standard). Sample id CytAssist_FFPE_Human_Lung_Squamous_Cell_Carcinoma. Spatial coordinates for Visium spots were extracted from the Seurat object and each spot was annotated with their transcription phenotype as *TYMS*$^{+}$*TK1*$^{+}$, *TYMS*$^{+}$*TK1*$^{-}$, *TYMS*$^{-}$*TK1*$^{+}$, or *TYMS*$^{-}$*TK1*$^{-}$ depending on the expression of TYMS and TK1 genes. For every spot, the phenotypes of neighboring spots within a specified radius were counted using a fixed radius nearest neighbor method using the R dbscan package (*47*). For each phenotype, the mean number of neighbors was calculated across all spots expressing that phenotype. The neighborhood analysis was repeated for increasing radii (from 1 to 10) where the number of neighbors surrounding a given spot is calculated as Σ6n where n is the radius. Note that only those spots with complete neighbors (i.e. the number of neighbors must be equal to Σ6n, which is not the case with spots closer to the slide boundaries) were used for calculating the mean number of neighbors by phenotype; this was subsequently plotted as a percentage of cells of each phenotype surrounding a cell of given phenotype. Analysis was done in R v4.4 a.

Statistical analysis

All statistical analyses were performed using GraphPad Prism 10, unless stated otherwise. Comparison-groups are indicated either in the figures with lines or stated in the figure legends. P-values of statistical significance are illustrated as follows: *<0.05; **p<0.01; ***p<0.001, ns represents non-significant results. Each experiment is the representative of at least three independent repeats.

Main Figures

Figure 1

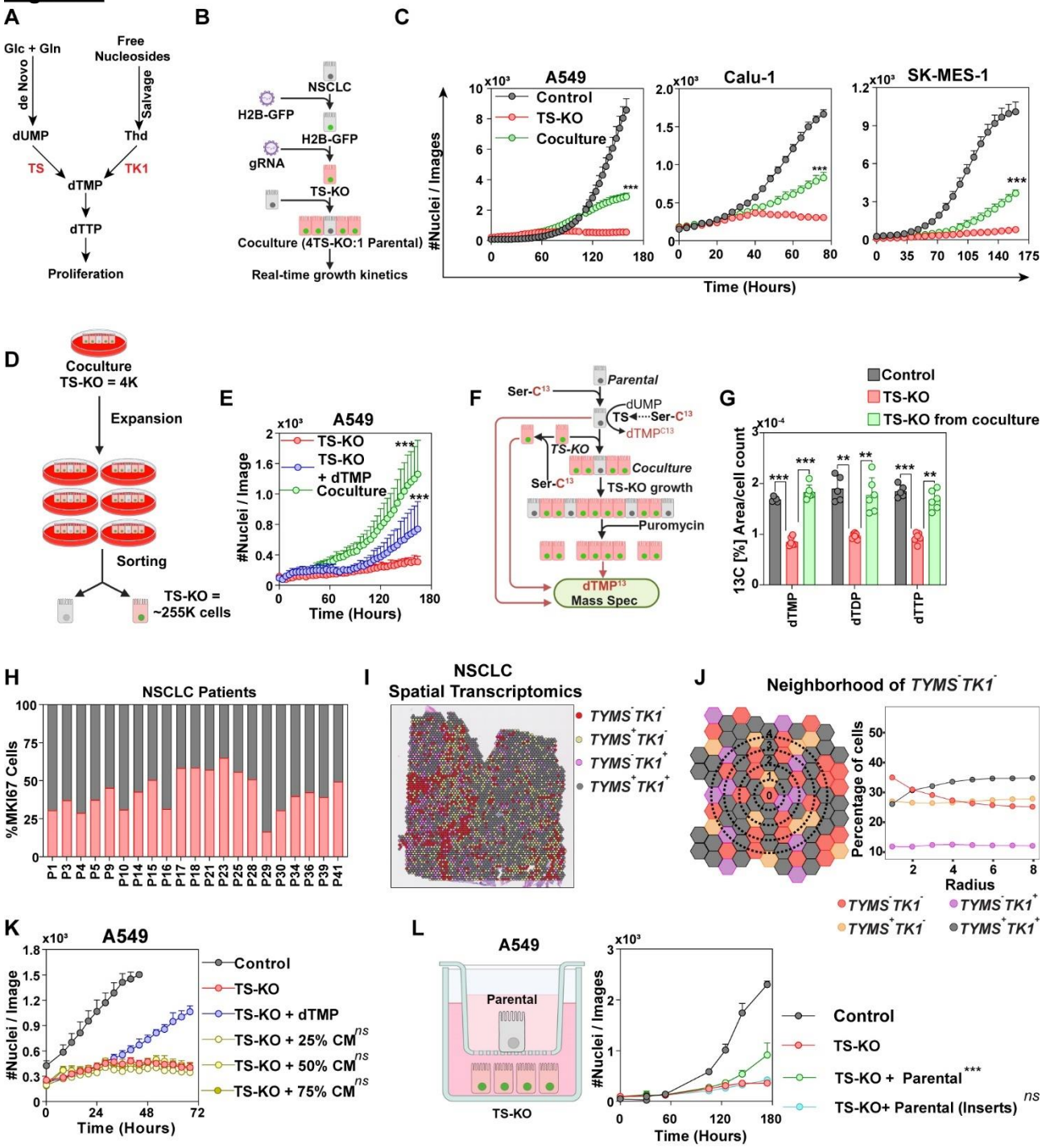

Figure 1. Thymidylate (dTMP) sharing in NSCLC cells.

(A) Cancer cells synthesize dTMP either de novo by assimilating glucose and glutamine and converting dUMP to dTMP by TS mediated enzymatic conversion, or by TK-1 mediated salvaging of free thymidine (Thd). **(B)** NSCLC cell lines (A549, Calu-1 and SK-MES-1)

850 expressing nuclear H2B-GFP, were knocked out for *TYMS* by CRISPR/Cas9 and cocultured
851 with their respective parental cells (expressing TS) in a ratio of 4:1. Proliferation of GFP^+
852 TS-KO cells was monitored using Incucyte S3. **(C)** The growth of TS-KO cells in coculture
853 with TS-expressing parental. As experimental controls, GFP-tagged cells were transduced
854 with vector containing a non-targeting sequence. The data are mean ± SD of three replicates
855 and the statistical test is a Two-Way ANOVA test with Tukey's multiple comparison test
856 correction. **(D)** A549 TS-KO cells were cocultured with parental cells for 10 passages and
857 sorted based on GFP expression. Cell counts at initial and final passage are indicated. **(E)**
858 Sorted cells from (D) were seeded in a 96-well plate and their dependency on exogenous
859 dTMP was quantified. The data are mean ± SD of three replicates and statistical test is Two-
860 Way ANOVA test with Tukey's multiple comparison test correction. **(F)** A549 cells were
861 cocultured in DMEM supplemented with Serine-C^{13} for 24 hours to enrich the cells for
862 $dTMP^{C13}$ ($A549^{C13}$). Puromycin resistant A549 TS-KO cells were cocultured with $A549^{C13}$
863 parental cells and selected with puromycin after their growth. $dTMP^{C13}$, $dTDP^{C13}$ and,
864 $dTTP^{C13}$ were quantified in selected TS-KO cells. $A549^{C13}$ and TS-KO cells cultured in Ser^{C13}
865 for 24 hours were used as controls. See also the Extended Fig. 3. **(G)** Quantification of
866 dTMP, dTDP, and dTTP tagged with C^{13} in the cells from (F). Bars represent mean ± SD of
867 six replicates and statistical significance is calculated by One-Way ANOVA with Sidak's
868 multiple comparison. **(H)** Single-cell transcriptomic data from NSCLC patients showing
869 contribution of cells lacking expression of *TYMS* and *TK1* (*$TYMS^-TK1^-$*) to the growth of
870 tumors. *$MKI67^+$* proliferative cells in *$TYMS^-TK1^-$* population were compared to other
871 populations (*$TYMS^+TK1^-$*, *$TYMS^-TK1^+$* and *$TYMS^+TK1^+$*) for 21 patients (with at least 50
872 proliferative cells). Each bar represents a single patient. See also Extended Fig. 4. **(I)** Spatial
873 transcriptomics data from a NSCLC biopsy, showing dispersion of *$TYMS^-TK1^-$* cells with
874 population with other genotypes. *$TYMS^+TK1^+$* = 1763 cells, *$TYMS^+TK1^-$* = 1000 cells, *$TYMS^-$*
875 *$TK1^+$* = 438 cells, *$TYMS^-TK1^-$* = 657 cells. **(J)** Neighborhood analysis of spatial
876 transcriptomics data from (G). Taking *$TYMS^-TK1^-$* cells as center, percentages of different
877 cell populations were calculated in successive radii. Percentages at each radius for each
878 *$TYMS^-TK1^-$* cell was averaged and represented as a dot, representing tendency of a cell
879 population to be located around these cells. **(K)** Proliferation kinetics of A549 TS-KO cells
880 showing their inability to proliferate with supplementation of condition medium from A549
881 parental cells cultured for 48 hours. Each point represents mean ± SD of three replicates,

882 statistical test is Two-Way ANOVA with Tukey's multiple comparison. **(L)** Lack of growth of
883 TS-KO cells in medium that is shared with the parental donor cells that were seeded on a
884 transwell chamber, physically separating them from the TS-KO cells. Each point represents
885 mean ± SD of three replicates, statistical test is Two-Way ANOVA with Tukey's multiple
886 comparison.

Figure 2

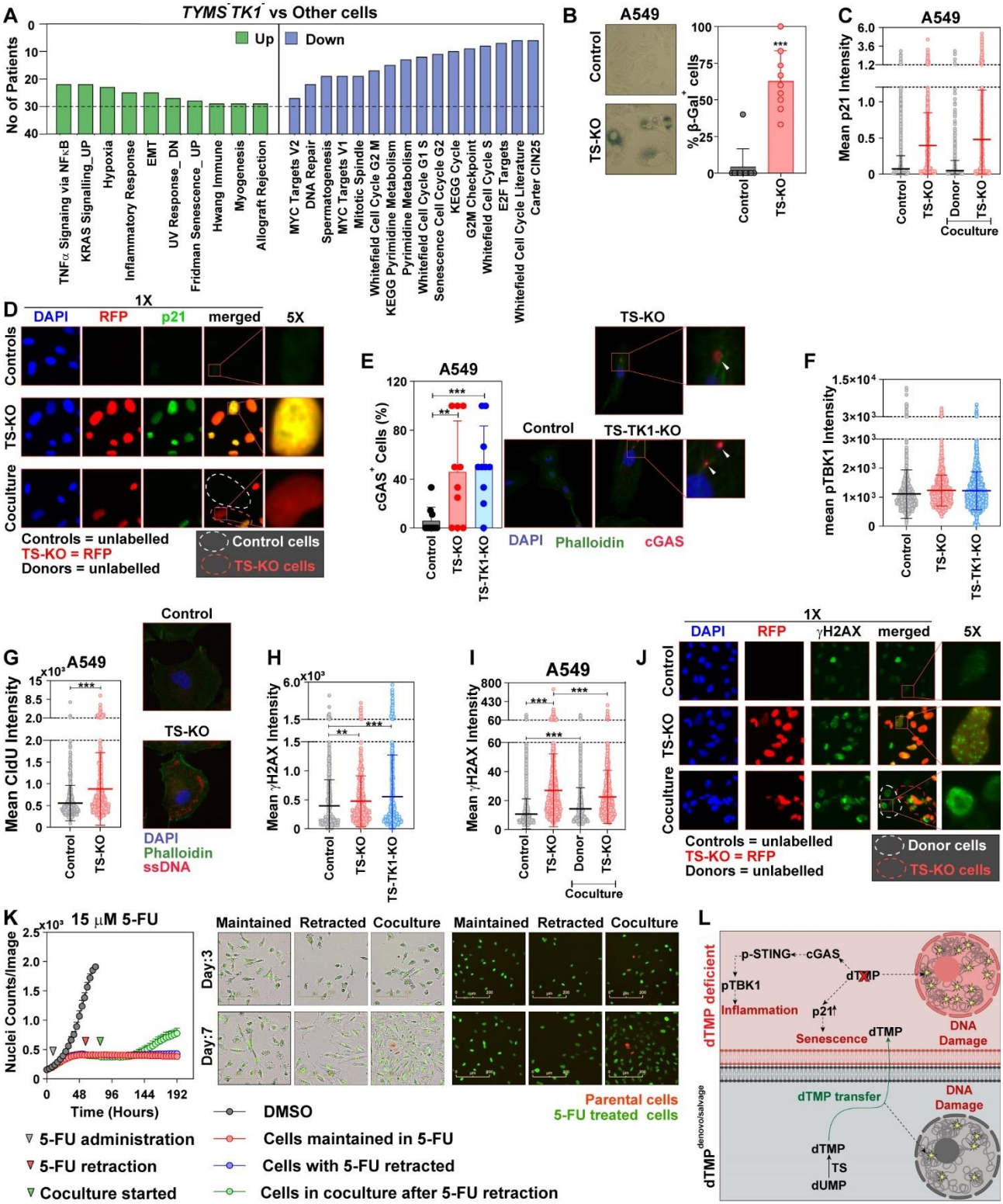

887

888

889

890 **Figure 2. dTMP deficiency is associated with key pathophysiological features of**
891 **cancer.**
892 **(A)** Pathways that are differentially regulated between *TYMS*$^{-}$*TK1*$^{-}$ cells and other
893 populations from cancer cells of NSCLC patients' scRNA seq (Extended Fig 4). Only those
894 pathways that were significantly regulated in more than 10 patients are included. **(B)** β-
895 galactosidase staining in A549 TS-KO cells compared to controls, showing increased
896 senescence in cells with TS-KO along with quantification of positive cells from the
897 representative images. Bar represents mean ± SD of cells counted from 10 images;
898 statistical analysis is Student's t-Test. **(C-D**) Quantitative-image-based cytometry (QIBC)
899 showing quantification of mean p21 expression (represented as mean intensity of
900 immunofluorescent labelled p21 normalized to nucleus size) in A549 TS-KO cells with
901 growth defect or in collective proliferation in coculture with parental A549 cells as donor
902 (along with representative images). Each dot represents the mean intensity of p21 in a single
903 cell, the longer line represents mean and shorter lines represent SD. Statistical analysis is
904 Student's t-Test. **(E)** Immunofluorescent staining of activated ssDNA-sensor cGAS in A549
905 cells with dTMP deficiency. Insets show cGAS signaling from cytoplasmic nuclear bodies,
906 indicated with white arrows. Bars represent mean ± SD of cGAS^{+} cells counted from 10
907 images and normalized to the total cell counts/image. Statistical analysis is Student's t-Test.
908 **(F)** QIBC showing increase of p-TBK1, which is the effector protein of cGAS-STING
909 pathway, significantly increased in cells with dTMP deficiency. Dots represent the mean
910 intensity of p-TBK1/cells, the longer line represents mean and shorter lines represent SD.
911 Statistical analysis is Student's t-Test. Please see the representative images in the Extended
912 Fig. 6I. **(G)** QIBC quantification of ssDNA in TS-KO cells quantified after staining with CldU.
913 Dots represent the mean intensity of CldU/cell, the longer line represents mean and shorter
914 lines represent SD. Statistical analysis is Student's t-Test. **(H)** Quantitation of DNA damage
915 marker γH2AX/cell in TS-KO A549 cells as quantified by QIBC. Dots represent cells, the
916 longer line represents mean and shorter lines represent SD. Statistical analysis is Student's
917 t-Test. **(I-J)** Quantitation of γH2AX/cell in TS-KO A549 cells in coculture with donor parental
918 cells, showing increased DNA damage in the donor parental cells in coculture compared to
919 the controls. Dots represent cells, the longer line represents mean and shorter lines
920 represent SD. Representative images and 5X zoom in the inset show increased γH2AX in
921 parental cells marked by white broken lines. Statistical analysis is student's t-Test. **(K)** Real-

time proliferation of A549 cells treated with sublethal doses of 15 μM 5-FU (TS inhibitor), which ablates the growth of cells. Parental cells were added to the coculture after drug retraction showing that 5-FU induced growth arrest could be restored by coculture with parental cells. Data is mean ± SD of three replicates. Significance is calculated by two-Way ANOVA with Tukey's multiple comparison. **(L)** Schematic representation of the pathophysiological features of dTMP deficient cells. Loss of dTMP leads to activation of DNA damage, senescence via p21 activation, and inflammation via cGAS-STING pathway. During collective proliferation, dTMP is passed from donor parental cells to dTMP deficient cells, creating DNA damage in the donor cells.

Figure 3

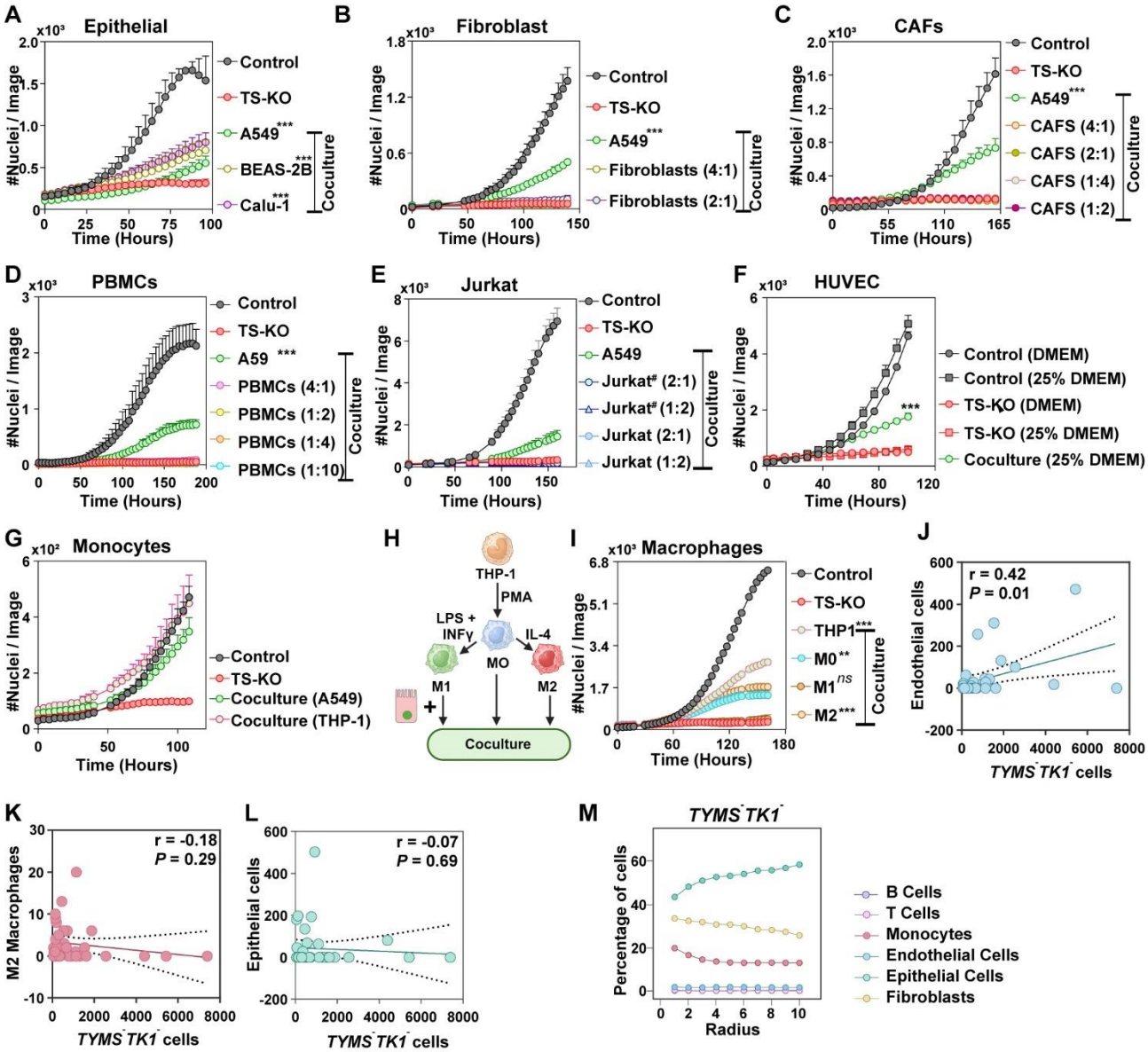

933

934 **Figure 3. The contribution of tumor microenvironmental (TME) cells to collective**
935 **proliferation.**

936 **(A)** Proliferation kinetics of A549 TS-KO in coculture with Calu1 and BEAS2B, showing that
937 collective proliferation can be coordinated between a LUSC cell line (Calu-1), a non-
938 cancerous cell line of epithelial origin (BEAS2B), and an LUAD cell line (A549). **(B-C)**
939 Coculture of A549 TS-KO cells with normal fibroblast cells and cancer associated fibroblasts
940 (CAFs). **(D)** A549 TS-KO cells cocultured with peripheral blood mononuclear cell (PBMCs),
941 that is highly enriched in lymphocytes. **(E)** Proliferation curve showing inability of either
942 activated (Jurkat#) or activated Jurkat cells to re-establish growth of A549 TS-KO cells. **(F)**

943 Proliferation curve showing human umbilical vein endothelial cells (HUVEC) supporting
944 collective proliferation of A549 TS-KO cells. **(G)** A549 TS-KO cells undergoing collective
945 proliferation in presence of THP-1 cells of monocytic lineage. **(H)** A scheme showing
946 induction of THP-1 monocytes to macrophage with different polarization. **(I)** Coculture of
947 A549 TS-KO with unpolarized M0 macrophages, M1 macrophages, or M2 macrophages
948 lineages from (H), showing collective proliferation being supported by all macrophages
949 except the M1 type. **(J-L)** Correlation between number of different TME cells (endothelial
950 cells, M2 macrophages and epithelial cells) and *TYMS*$^{-}$*TK1*$^{-}$ cells from scRNA data from
951 Extended Fig. 4. Correlation is calculated by Pearson's rank correlation. **(M)** Neighborhood
952 analysis showing increased propensity of *TYMS*$^{-}$*TK1*$^{-}$ cells to be in neighborhood of
953 epithelial cells. In experiments (A-I) data points represent mean ± SD for three replicates
954 and the statistical test is Two-Way ANOVA with Tukey's multiple test.
955
956

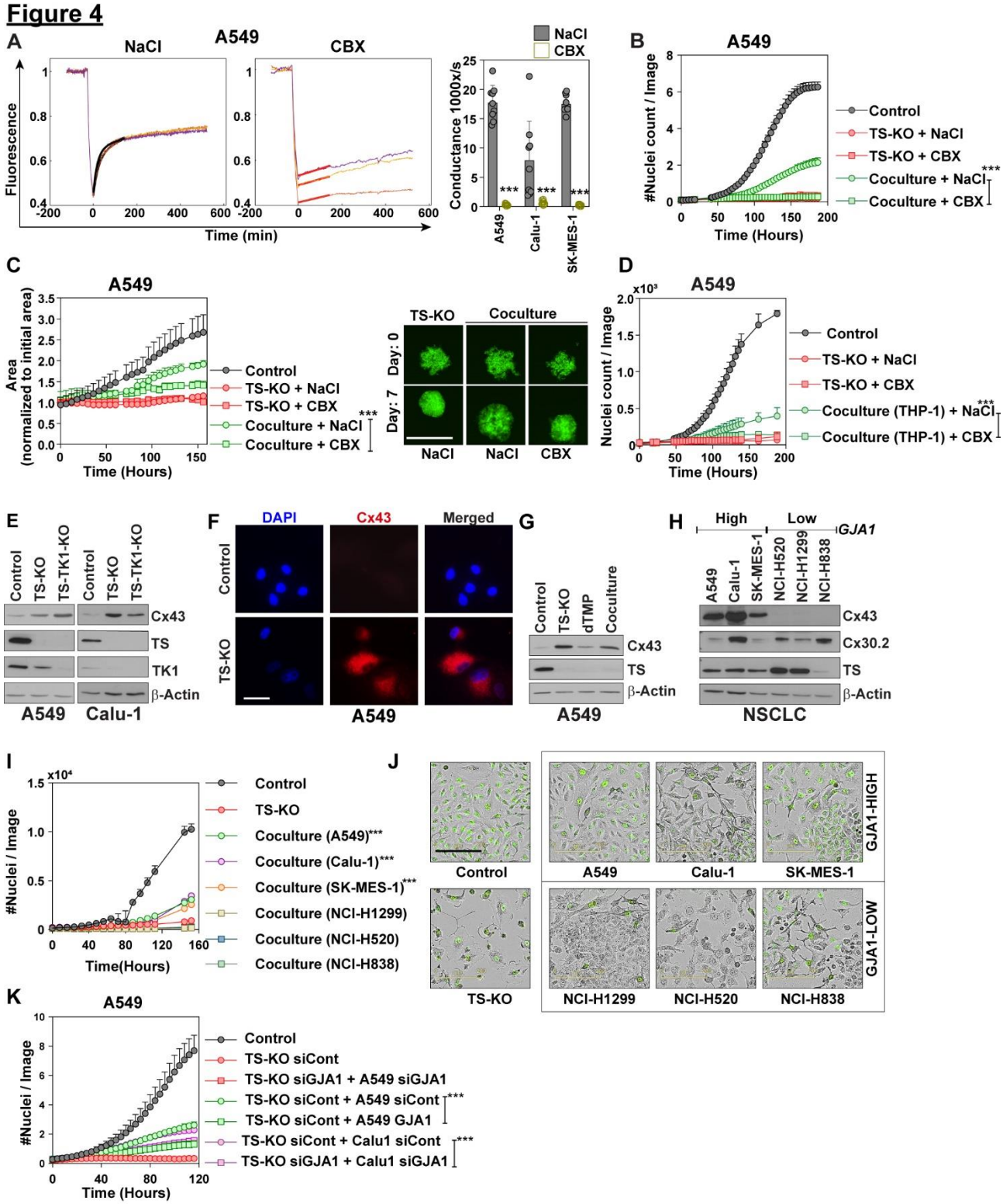

Figure 4. Gap-junctions (GJs) mediate dTMP sharing.

(A) Fluorescence recovery after photobleaching (FRAP) showing connectivity of indicated cells, measured by their ability to reconstitute fluorescent dye after bleaching, in presence

961 of either NaCl or 100 μM of the gap junction inhibitor Carbenoxolone (CBX). Each bar
962 represents the mean ± SD of 10 replicates. Significance is determined using One-Way
963 ANOVA analysis. Fluorescence recovery for for Calu-1 and SK-MES-1 cells are shown in
964 Extended Fig. 8B. **(B)** Incucyte proliferation assay measuring growth of A549 TS-KO cells
965 in coculture with parental A549 cells in presence of either 100 μM CBX or NaCl. Significance
966 is determined using a Two-Way ANOVA analysis with Tukey's multiple comparison. **(C)**
967 Collective growth of TS-KO cells, as grown in 3D-spheroids, in presence of either 100 μM
968 CBX or NaCl. Images for spheroids showing GFP signal, scale bar represents 800 μm. Each
969 point represents the mean ± SD of five replicates. Significance is determined using a Two-
970 Way ANOVA analysis with Tukey's multiple comparison. See representative images of
971 control and TS-KO spheroids in Extended Fig. 8G. **(D)** Collective growth of TS-KO cells in
972 presence of THP-1 monocytes abrogated by supplementation of 100 μM CBX compared to
973 NaCl. The data are mean ± SD of 3 replicates. Significance is determined using a Two-Way
974 ANOVA analysis with Tukey's multiple comparison. **(E)** Increased expression of Cx43
975 proteins, which hexamerizes to form GJA1 quantified in TS-KO and TS-TK1 KO cells. **(F)**
976 Immunofluorescence images showing increase of Cx43 (the protein coded by GJA1) in TS-
977 KO cells. Scale bar represents 200 μm **(G)** Quantification of Cx43 in proliferative A549 TS-
978 KO cells compared to the controls and non-proliferative TS-KO cells. **(H)** NSCLC cell lines
979 classified high and low based on the expression of *GJA1* (Cx43). **(I)** The inability of *GJA1*
980 low cells to promote collective growth in TS-KO cells, as quantified by Incucyte S3. The data
981 are mean ± SD of three replicates. Significance is determined using a Two-Way ANOVA
982 analysis with Tukey's multiple comparison. Significance is compared to the TS-KO cells. **(J)**
983 Representative images from (I) showing that TS-KO cells failed to restore their normal
984 morphology when they were cocultured with *GJA1*-Low cells. Scale bar represents 200 μm.
985 **(K)** Simultaneous siRNA (80 nM) mediated knockdown of *GJA1* in A549 TS-KO and parental
986 cells, and its abrogative effect on collective growth. The data are mean ± SD of three
987 replicates. Significance is Two-Way ANOVA with Tukey's multiple comparison.
988

Figure 5

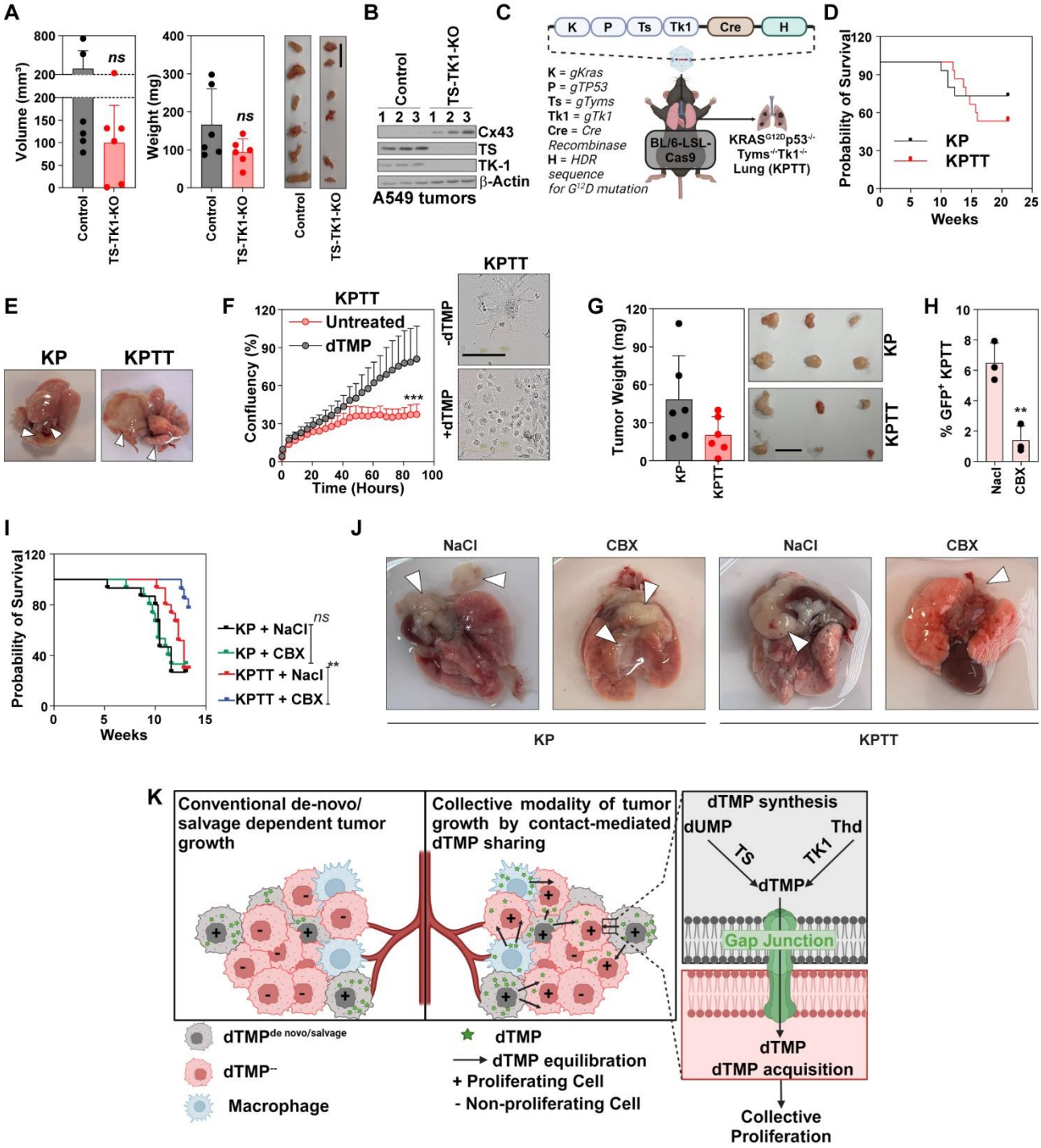

Figure 5. Gap junction dependent growth of dTMP-deficient growth of NSCLC tumors. (A) Weights and volumes of tumor formed from A549 TS-TK1-KO cells in flanks of NSG mice along with the pictures of excised tumors. TS-TK1-KO tumors were excised five days after the controls. Bars are mean ± SD of tumors from 6 flanks of 3 mice and significance is calculated by Student's t-Test. Scale bar represents 1 cm. **(B)** Westen blot quantification of

995 TS and TK1 in tumors excised from (A) showing depletion of TS and TK1 proteins and
996 increased expression of Cx43 (*GJA1*) in TS-TK1-KO cells**. (C)** C57BL/6 expressing Cas9
997 were intubated with AAV9 vectors carrying gRNA for *Kras* (along with G12D HDR sequence),
998 *p53*, *Tyms,* and *Tk1* resulting in lung specific mutations in targeted genes. Intubated mice
999 develop $Kras^{G12D}$ and $p53^{-/-}$ driven tumors that lack expression of *Tyms* and *Tk1* genes,
1000 resulting in KPTT tumors. **(D)** Comparison of tumors formed by mice harboring tumor
1001 specific mutation in lungs of C57BL/6 mice. KP ($Kras^{G12D}$ $p53^{-/-}$) mice have been used as
1002 controls. **(E)** Representative images from lungs with tumors from the mice in (C). **(F)** Cell
1003 line established from KPTT tumor dependent on exogenous dTMP supplementation (10 μM)
1004 for proliferation and undergoing senescense-like enlarged phenotype in absence of dTMP.
1005 The data are mean ± SD of three replicates. Significance is Two-Way ANOVA with Tukey's
1006 multiple comparison. **(G)** Weight of tumors excised from subcutaneous implantation of KP
1007 and KPTT tumors in C57BL/6 along with representative images. Each bar represents the
1008 mean ± SD of tumors from 6 flanks of 3 mice. Significance is calculated by Student's t-Test.
1009 Scale bar represents 1 cm **(H)** Flow cytometry quantification of GFP^{+} KPTT cells cocultured
1010 with syngeneic Ladi 2.1 cells derived from a lung tumor of a C57BL/6 mouse. Cocultures
1011 were treated either with 100 μM CBX or the vehicle control. The bars are mean ± SD of three
1012 replicates and significance is calculated by Student's t-Test. **(I)** Survival of KPTT mice
1013 compared to KP mice when treated with 40 mg/kg CBX or corresponding volume of the
1014 vehicle control NaCl. (n = 15 for all the groups except the KPTT + CBX where n = 14).
1015 Statistic is calculated by Log-Rank (Mantel Cox) test. **(J)** Images of lung with tumors from
1016 (H). KPTT+CBX lungs are from the same week of the representative KPTT + NaCl lung, at
1017 the time of the termination of experiment. **(K)** The current model of proliferation relies on
1018 activation of canonical *de novo* and/or salvage pathways in each proliferating cell, whereas
1019 the model of collective proliferation postulates that growth is a cumulative sum of
1020 proliferation of cells with *de novo* and salvage and cells that rely of dTMP sharing via gap
1021 junctions.
1022

Extended Figures

Extended Figure 1

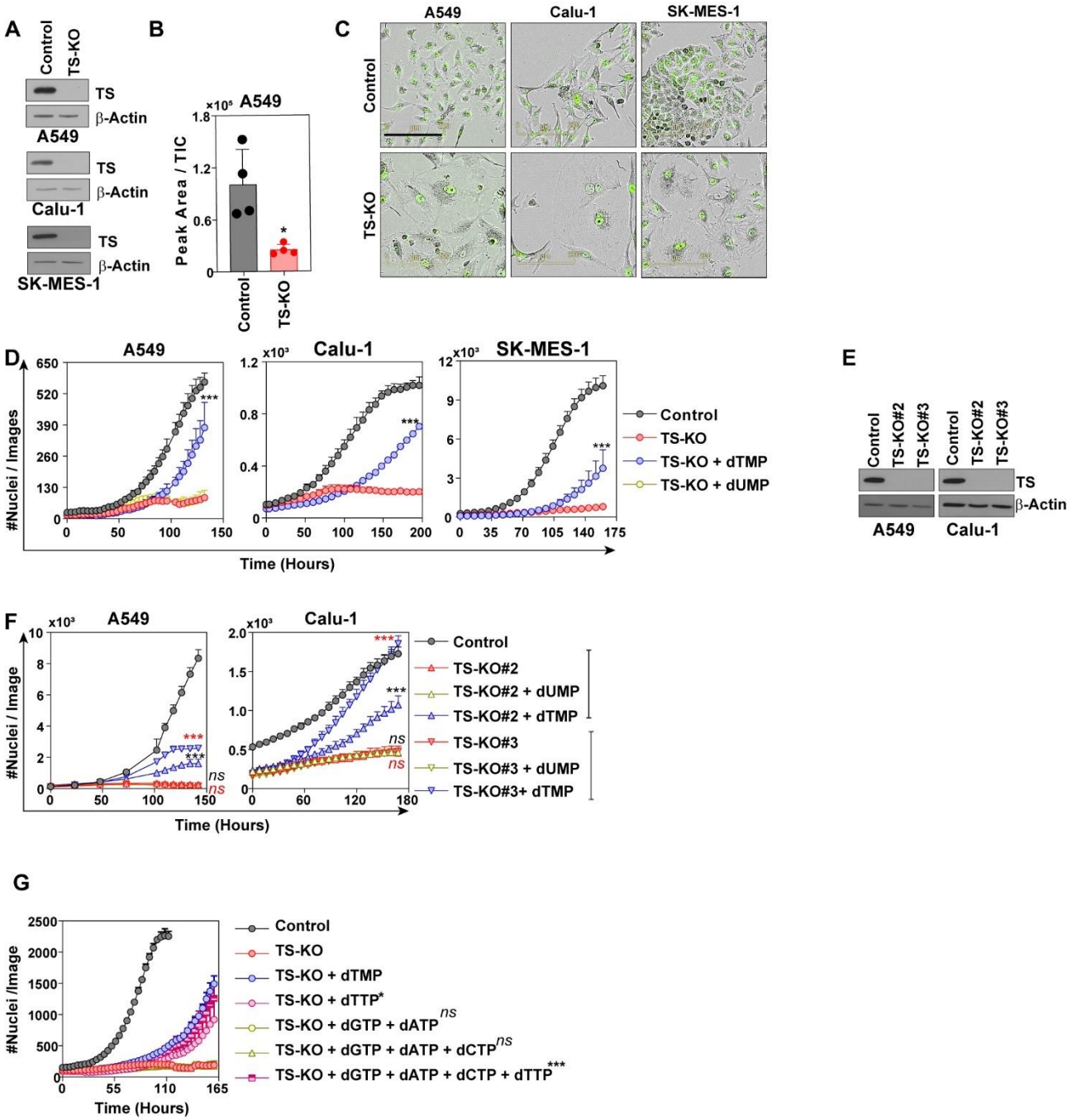

Extended Fig. 1. de novo deficient model dependent on exogenous dTMP. **(A)** Western blot quantification of TS-KO in indicated cell lines. **(B)** Mass-spec quantification of dTMP in A549 TS-KO cells compared to the control cells. Each bar represents mean ± SD of five replicates. Significance is calculated by Student's t-Test. **(C)** Images from (B) showing TS-KO cells with enlarged morphology. Scale bar represents 200 µm. **(D)** Growth

curve highlighting dependency of TS-KO cells on 10 μM dTMP supplementation in comparison to 10 μM dUMP (only A549). Significance is compared to TS-KO cells. Each point represents mean ± SD of three replicates. Significance is Two-Way ANOVA and Tukey's Multiple Test. **(E)** KO of TS with non-overlapping gRNAs for *TYMS* other than what has been shown in Fig 1C and Extended Fig. 1A. **(F)** Treatment of the cells in (E) with 10 μM dTMP and 10 μM dUMP. Each point represents mean ± SD of three replicates. Significance compared to TS-KO calculated by Two-way ANOVA and Tukey's Multiple Test. (**G**) Treatment of TS-KO cells with different combination of dNTPs, showing that only dTTP supplementation has positive effect on their growth. Each point represents mean ± SD of three replicates. Significance compared to TS-KO calculated by Two-way ANOVA and Tukey's Multiple Test.

1043

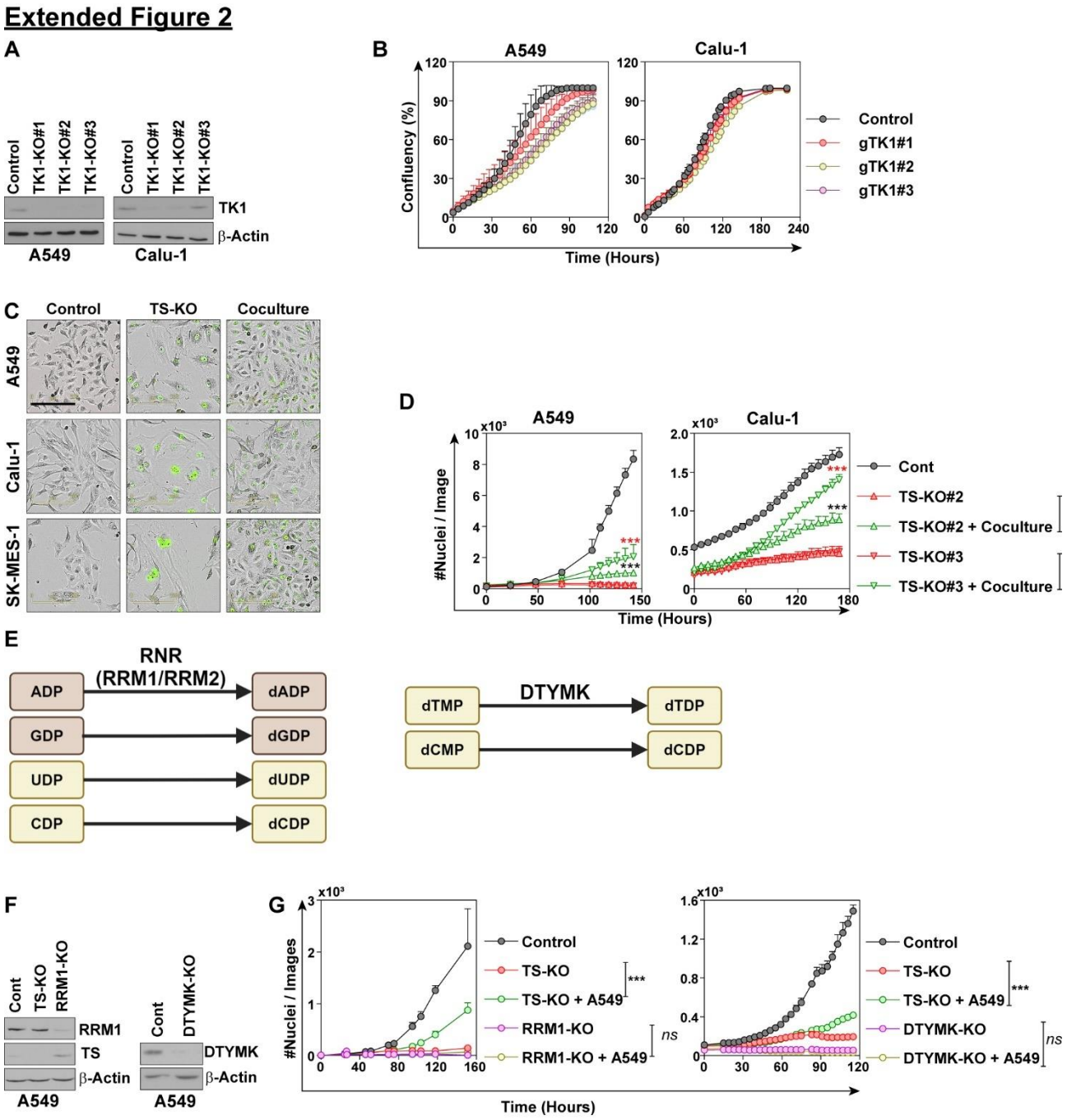

1044

1045 **Extended Fig. 2. Collective proliferation is restricted to transfer of dTMP.**

1046 **(A)** Western blot depicting CRISPR/Cas9 mediated knockout of *TK1* using multiple
1047 sequences in A549 and Calu-1 cells. **(B)** Proliferation curve showing growth in TK1-KO cells
1048 compared to the controls. Each point represents mean ± SD of three replicates. **(C)** Images
1049 from Fig. 1C showing that TS-KO cells regain normal morphology in coculture with parental
1050 cells. Scale bar represents 200 μm. **(D)** Rescue of the growth arrest of A549 and Calu-1

1051 cells knocked out with two independent gRNAs, other than that shown in the Fig. 1C.
1052 Significance, compared to TS-KO, is Two-way ANOVA with Tukey's multiple comparison.
1053 Each point represents mean ± SD of three replicates. **(E-F)** Western blot quantification of
1054 *RRM1* and *DTYMK* KO in A549 to deplete all dNTP and pyrimidine deoxyribonucleotides
1055 respectively. **(G)** Growth curve quantifying the proliferation of cells in coculture with parental
1056 A549 cells after *RRM1*- and *DTYMK1*-KOs. Each point represents mean ± SD of three
1057 replicates. Significance compared between cocultures and their respective controls by Two-
1058 way ANOVA with Tukey's multiple comparison.
1059
1060

Extended Figure 3

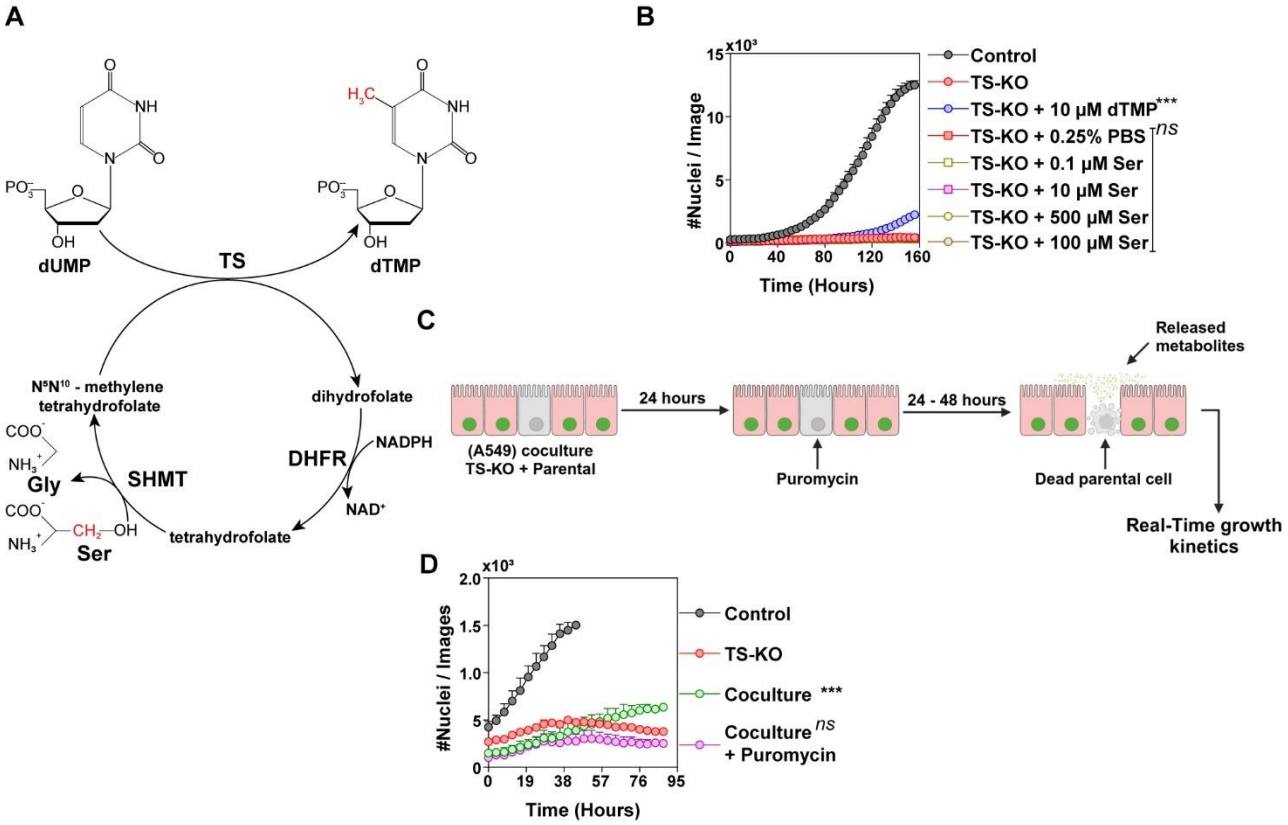

Figure S3. Serine as a source of dTMP detection.

(A) TS-coupled folate cycle highlighting transfer of methyl group (red) from serine to dUMP for synthesis of dTMP. C13 labeled serine was used for detection of dTMP by mass spectroscopy shown in the Fig. 1F-G. **TS** = thymidylate synthase**, DHFR** = dihydrofolate reductase**, SHMT** = serine hydroxymethyl transferase. **(B)** Proliferation curve showing that serine did not directly contribute to support the growth of TS-KO cells. Significance is compared to TS-KO. Each point represents mean ± SD of three replicates. **(C)** Scheme depicting the proliferation kinetics of TS-KO cells in presence of parental cells treated with puromycin. **(D)** Proliferation curve showing that puromycin-killed parental cells did not contribute to the growth of TS-KO cells. Each point represents mean ± SD of three replicates. Significance is compared to TS-KO. Significance calculated in by Two-Way ANOVA with Tukey's multiple comparison.

1077

Extended Figure 4

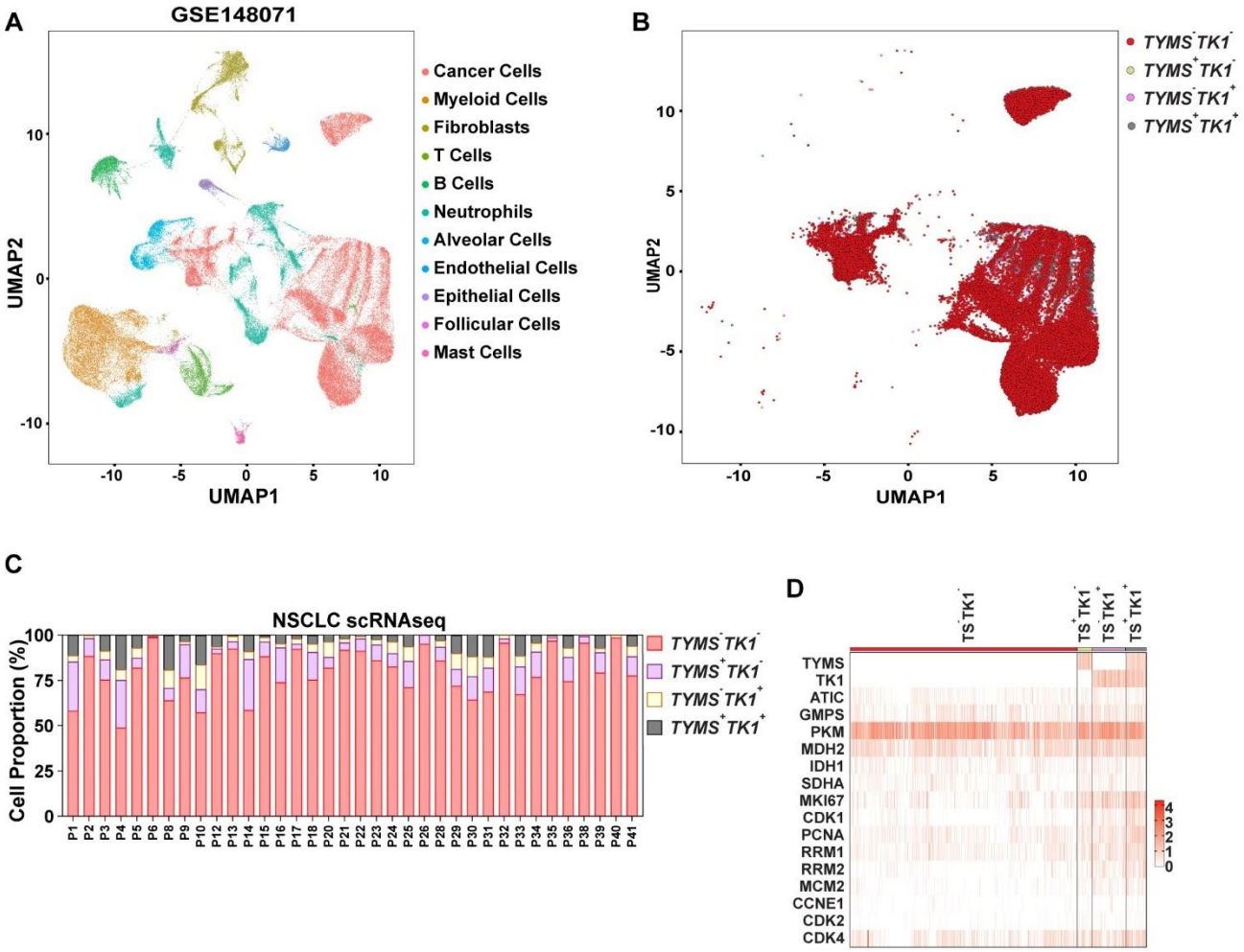

1078

1079 **Extended Fig. 4. Quantification of *TYMS-TK1-* cells in scRNA seq DNA of NSCLC**
1080 **patients.**

1081 **(A)** Single cells from 40 NSCLC patients clustered into different cell types (n = 40). Each dot
1082 represents a single cell. The number of cells is 88,672. **(B)** Representation of cells with both
1083 *de novo* (*TYMS*$^{+}$*TK1*$^{+}$), only *de novo* (*TYMS*$^{+}$*TK1*$^{-}$), only salvage (*TYMS*$^{-}$*TK1*$^{+}$) or neither
1084 (*TYMS*$^{-}$*TK1*$^{-}$*)* from cell types clustered from single cell data for 40 NSCLC patients. Each dot
1085 represents a cancer cells. The number of cancer cells is 39,787. **(C)** Patient-wise distribution
1086 of different population from (B). Each bar represents a single patient. **(D)** Expression of
1087 indicated metabolic genes and proliferation markers in TYMS^{-}TK1^{-} cancer cells from 40
1088 patients from (A) compared to other cell populations. *TYMS* = Thymidylate Synthase, *TK1*=
1089 Thymidine Kinase-1, Purine metabolism genes (*ATIC* = 5-Aminutesoimidazole-4-
1090 Carboxamide Ribonucleotide, *GMPS* = Guanine Monophosphate Synthase), glycolysis

genes (*PKM* = Pyruvate Kinase M1/2), tricarboxylic acid cycle (MDH2 = Malate Dehydrogenase – 2, *IDH1* = Isocitrate Dehydrogenase (NADP(+))-1, *SDHA* = Succinate Dehydrogenase Complex Flavoprotein Subunit A), proliferation genes (*MKI67* = Marker Of Proliferation Ki-67, *CDK1* = Cyclin Dependent Kinase 1, *PCNA* = Proliferating Cell Nuclear Antigen, *RRM1* = Ribonucleotide Reductase Catalytic Subunit M1, *RRM2* = Ribonucleotide Reductase Catalytic Subunit M2, *MCM2* = Minichromosome Maintenance Complex Component 2, *CCNE1* = Cyclin E1, *CDK2* = Cyclin Dependent Kinase 2, *CDK4* = Cyclin Dependent Kinase 4).

Extended Figure 5

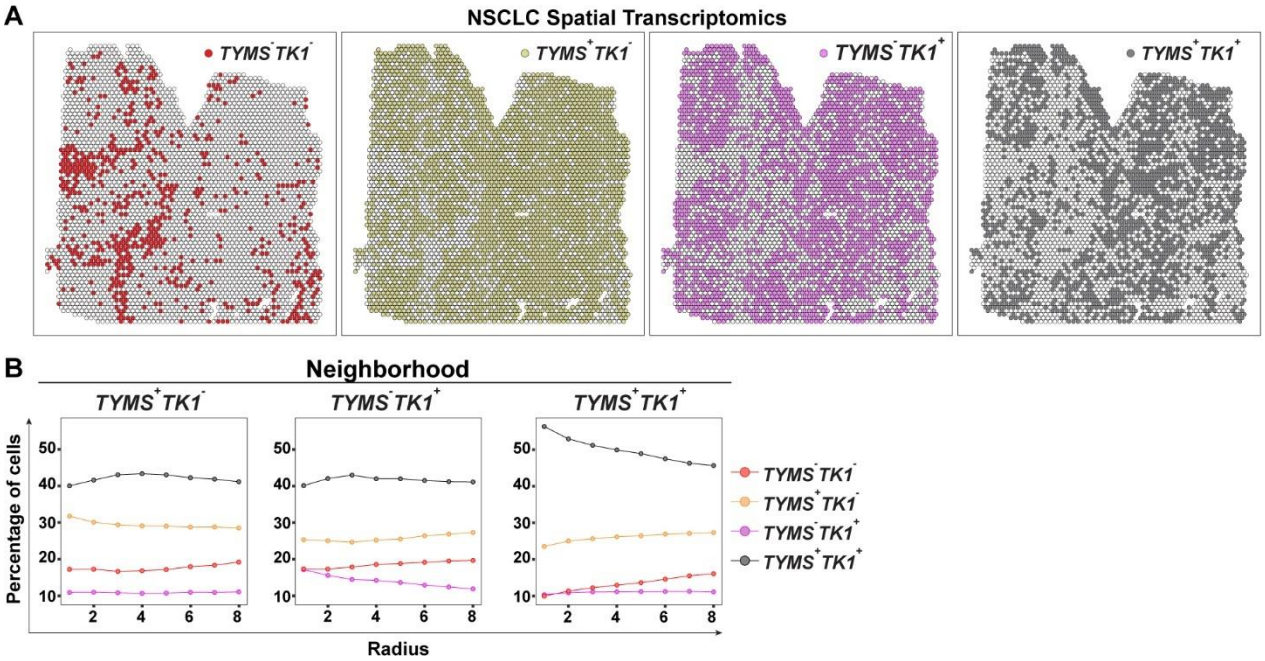

Extended Fig. 5. Spatial distribution of cells based on expression of *TYMS* and *TK1*. **(A)** Spatial distribution of indicated populations from Fig. 1I shown in individual map. **(B)** Neighborhood analysis of indicated population. See Fig. 1J.

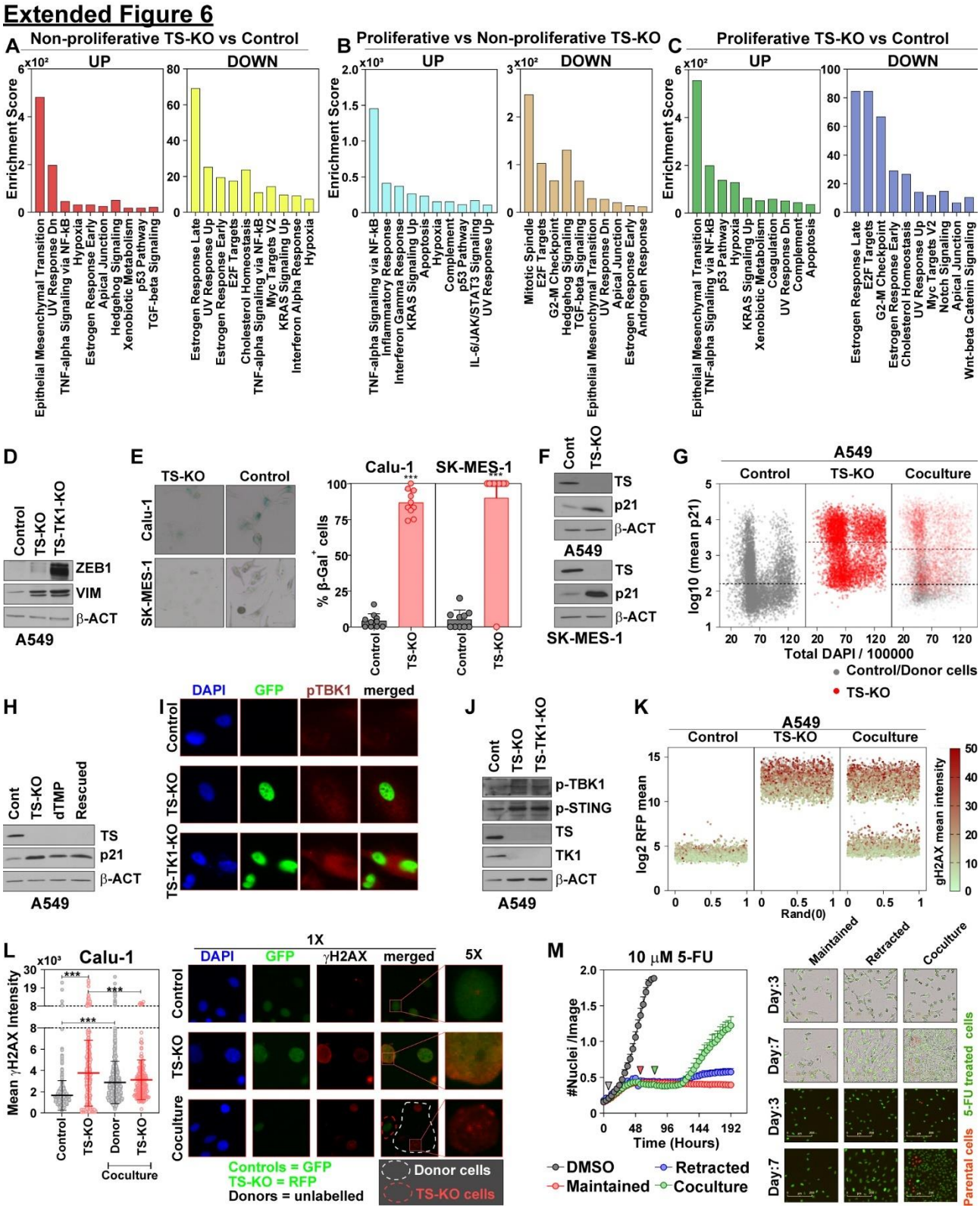

Extended Fig. 6. Pathophysiological features associated with collective proliferation.

(A-C) Transcriptomic changes were globally analyzed in TS-KO cells and showing **(A)** Differentially regulated pathways in TS-KO cells compared to control cells**, (B)** differentially

1113 regulated pathways in proliferative TS-KO cells (that were collected from coculture after
1114 puromycin induced death of parental donors) and non-proliferative TS-KO cells, and **(C)**
1115 differentially regulated pathways between proliferative TS-KO cells and control cells. **(D)**
1116 Western blot showing increased quantification of EMT makers in A549 cell line with dTMP
1117 deficiency. **(E)** Quantification of β-galactosidase, a marker of senescence in Calu-1 and SK-
1118 MES-1 cells. Bars represent mean ± SD of cells counted from 10 image fields. Statistical
1119 test is Student's t-Test. **(F)** Increased expression of p21 in cells with TS-KO, as quantified
1120 by western blot. **(G)** Distribution of p21 in single cells from Figure 2C based on the total
1121 intensity of DAPI. Broken lines represent medians. **(H)** Quantification of p21 in A549 TS-
1122 KO cells in non-proliferative and proliferative (Rescued) states. **(I)** Representative images
1123 from Fig. 2F showing increased pTBK1 in cells with dTMP deficiency. **(J)** Quantification of
1124 cGAS-STING the effector proteins p-STING and p-TBK1 in TS-KO A549 cells. **(K)**
1125 Distribution of cells expressing γH2AX in TS-KO cells in coculture, showing increased mean
1126 γH2AX in RFP negative parental donor cells from Figure 2I. **(L)** Quantitation of γH2AX/cell
1127 in Calu-1 cells with TS-KO in coculture with donor parental cells. Dots represent cells, the
1128 longer line represents mean and shorter lines represent SD. Representative images, and
1129 5X zoom in the inset show increased γH2AX in parental cells marked by white broken lines.
1130 Statistical analysis is Student's t-Test. **(M)** Real-time proliferation of A549 cells treated with
1131 10 μM 5-FU. Parental cells were added to the coculture after drug retraction showing that 5-
1132 FU induced growth arrest could be restored by coculture with parental cells. Grey arrowhead
1133 denotes the time of treatment, red arrowhead represents drug-retraction and green
1134 arrowhead indicates the time of coculture. Data is mean ± SD of three replicates.
1135 Significance is calculated by Two-Way ANOVA with Tukey's multiple comparison.
1136

Extended Figure 7

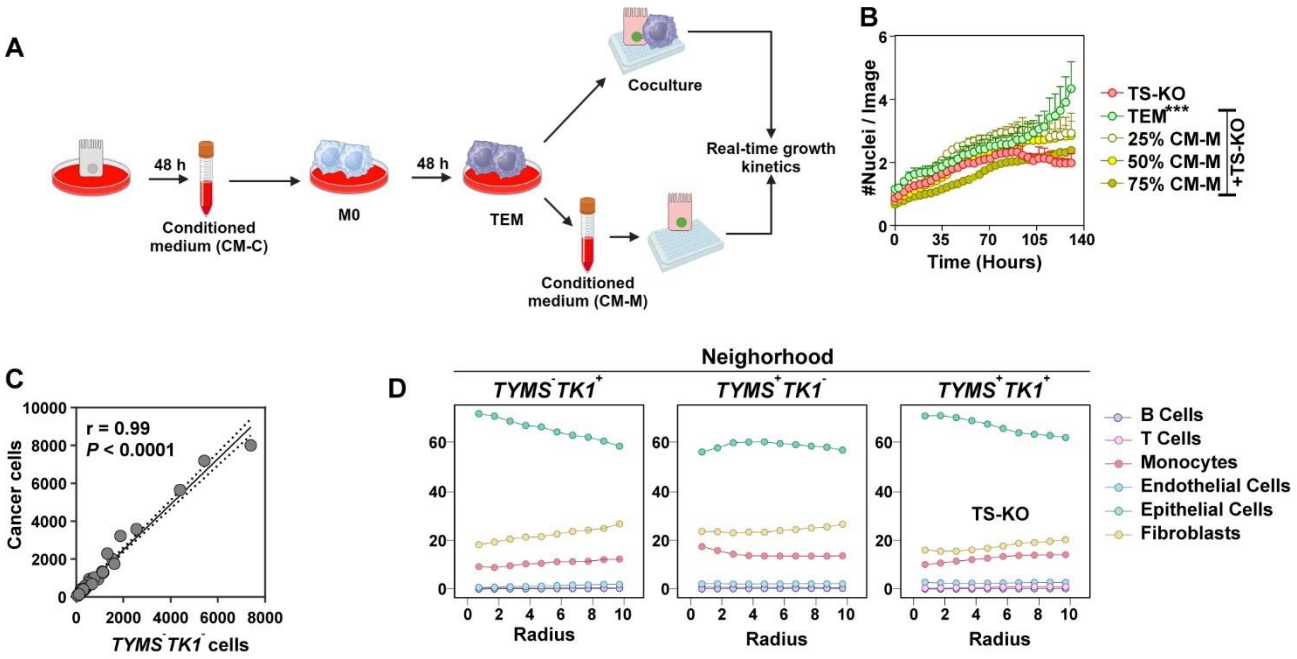

Extended Fig. 7. Contribution of tumor microenvironment (TME) cells to collective proliferation.

(A) Schematic representation of the workflow followed for educating of M0 macrophages with cancer cells. Condition medium (CM-C) was collected from A549 cells after 48 hours of seeding. M0 macrophages were treated with CM-C for 48 hours and conditioned medium, referred to as CM-M, was then collected from tumor educated macrophages (TEMs). **(B)** Proliferation curve showing that CM-M in (A) has no effect on the growth of TS-KO cells. Data is mean ± SD of three replicates. Significance is calculated by Two-way ANOVA with Tukey's multiple comparison. **(C)** Correlation between the numbers of total cancer cells and *TYMS*$^{-}$*TK1*$^{-}$ from combined pool of cancer cells from patients in Extended Fig. 4. **(D)** Neighborhood analysis depicting proximity of *TYMS*$^{-}$*TK1*$^{-}$ cells in Fig. 1I with different TME cells. See also Fig. 3M.

1152

Extended Figure 8

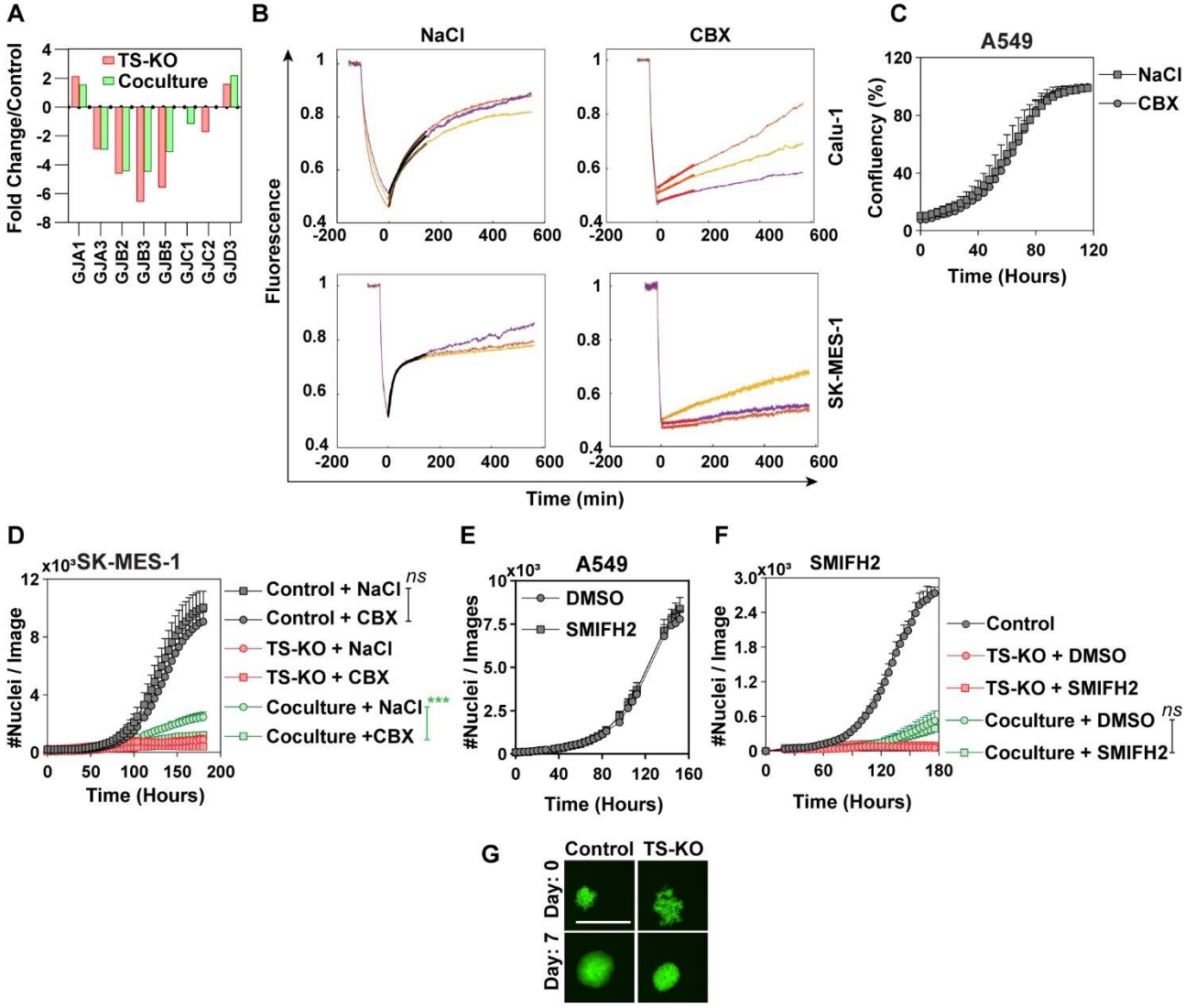

1153

1154 **Extended Fig. 8. Gap junction connects cells for collective proliferation.**

1155 **(A)** RNA sequencing analysis comparing TS-KO cells and puromycin selected TS-KO cells
1156 grown in coculture. GJA1 and GJD3 were two gap junction genes upregulated in both TS-
1157 KO and puromycin selected TS-KO cells. **(B)** Restoration of fluorescence in presence of
1158 either NaCl or CBX in Calu-1 and SK-MES-1 cell line from Fig 4A. **(C)** Proliferation curve
1159 showing that 100 μM CBX has no effect on the growth of A549 cells. **(D)** Collective
1160 proliferation reduced by 100 μM CBX in SK-MES-1 cells. Data is mean ± SD of three
1161 replicates. Significance is calculated by Two-Way ANOVA with Tukey's multiple comparison.
1162 **(E)** Treatment of A549 cells with 50 μM of F-actin inhibitor SMIFH2, showing no effect on
1163 the growth of cells. **(F)** Collective proliferation of A549 cells with TS-KO was not affected in

1164 presence of 50 μM SMIFH2. **(G)** Representative images from Figure 4C, showing reduction
1165 of spheroid formation in A549 TS-KO cells. Scale bar represents 200 μm. All significances
1166 are calculated by Two-Way ANOVA with Tukey's multiple comparison.
1167
1168

1169

Extended Figure 9

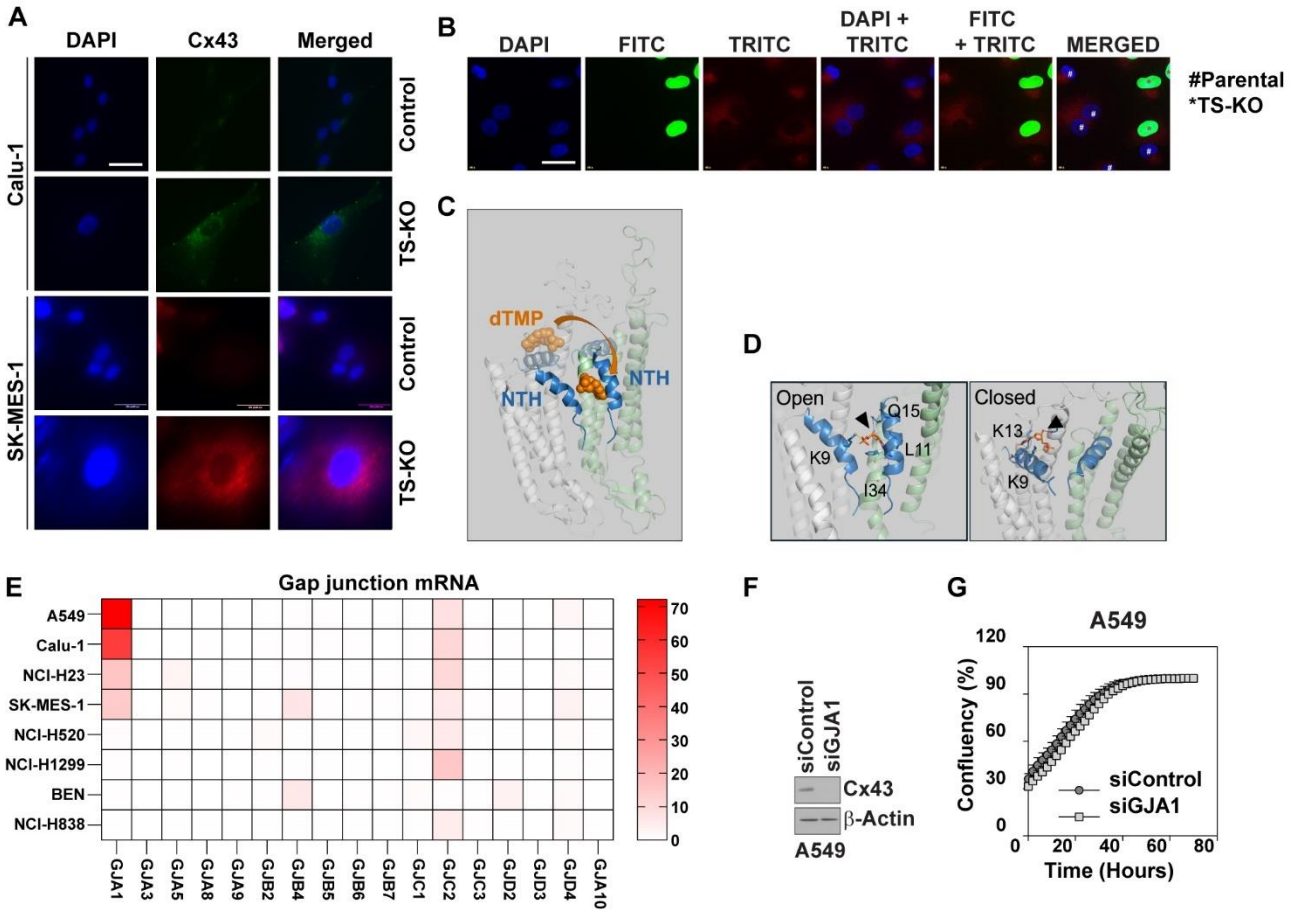

1170

1171 **Extended Figure 9. GJA1 is essential for collective proliferation.**

1172 **(A)** Increased expression of Cx43 (*GJA1*) in in indicated cell lines quantified by
1173 immunofluorescence. Scale bar represents 200 µm. **(B)** Immunofluorescence staining of
1174 Cx43 in GFP^{+} TS-KO cells and non-GFP parental cells, showing increased expression of
1175 GJA1 in parental cells. Scale bar represents 200 µm. **(C-D)** Autodock based prediction of
1176 dTMP binding to the open conformation of GJA1. 9th Lysine residue in Cx43 shows
1177 interaction with dTMP. Interactions have been indicated with black arrowheads. **(E)**
1178 Expression of GJA1 along with different gap junctions in selected NSCLC cell lines from
1179 CCLE data set. **(F)** Quantification of siRNA mediated knockdown of GJA1 in A549 cells.
1180 **(G)** Incucyte S3 quantification of proliferation in cells with GJA1 knockdown, showing that
1181 cells with siGJA1 in 4M has no proliferation defect. Each point represents mean ± SD of
1182 three replicates.

1183

1184

Extended Figure 10

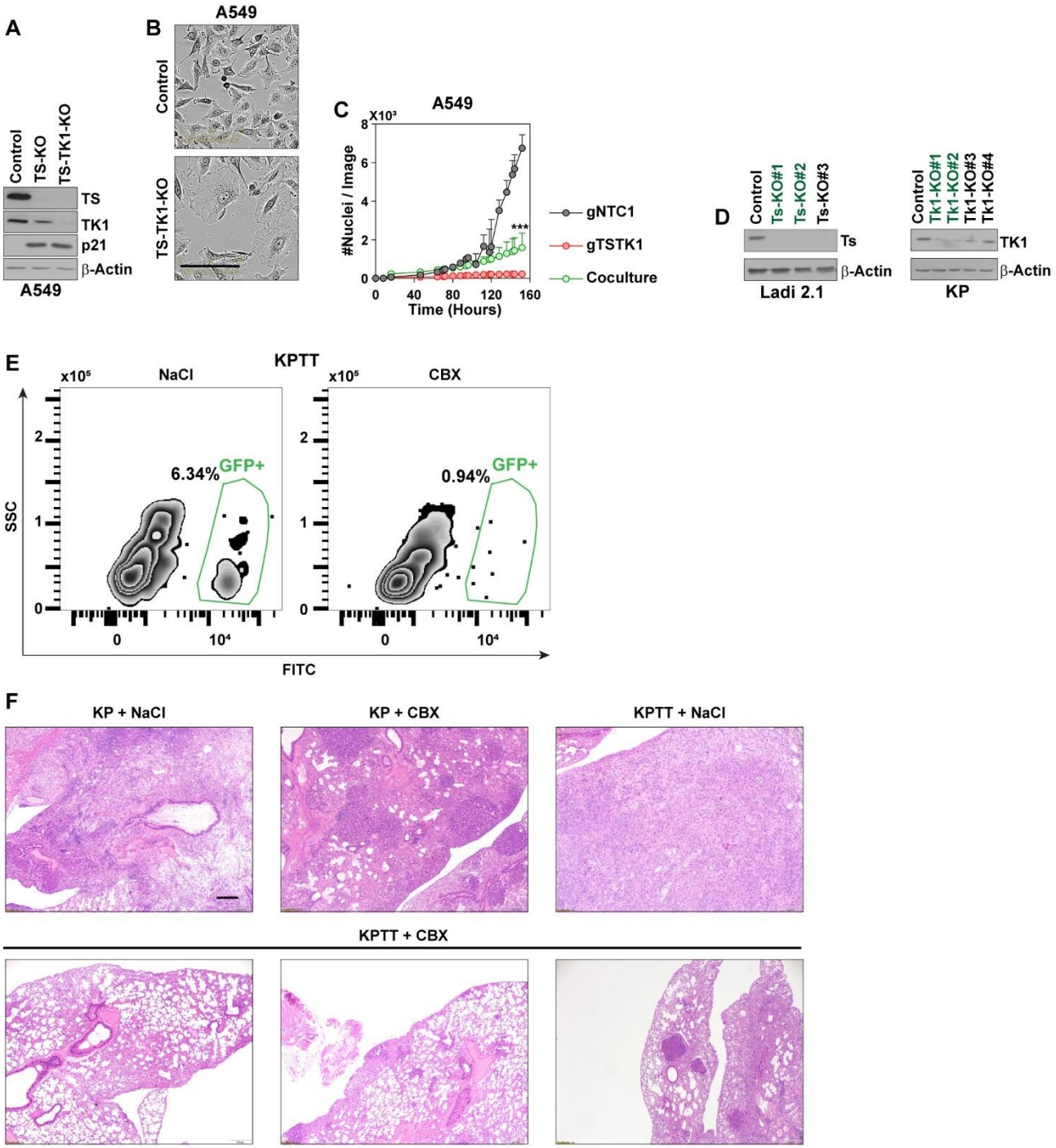

Figure S10. Growth of *TYMS*⁻*TK1*⁻ tumors are dependent on gap junctions.

(A) Generation of A549 TS-TK1-KO cells used in Figure 5A showing loss of TS and TK1 along with increased p21. **(B)** A549 TS-TK1-KO cells showing senescence-like enlarged and flattened morphology. Scale bar represents 200 µm. **(C)** Real-time proliferation curve showing dependence on TS-TK1-KO cells on parental cells for growth. **(D)** Western blot

showing quantification of Ts and Tk1 knockdown in cancer cells derived from C57BL/6 tumors. gRNAs #1 and #2, that are formatted in green, (both for Ts and Tk1) were used for generation of KPTT mice. (**E**) Flow cytometry quantification of GFP^+ KPTT cells from coculture with Ladi 2.1 (a syngeneic lung cancer cell line that was established from KP on C57BL/6 background) cells in presence of either NaCl or 100 μM CBX. Quantification is shown in Fig. 5H. **(F)** Representative H&E images of lungs from Fig 5J, showing the tumor load in each group. Scale bar represents 100 μm.

References

1 Ma, J. *et al.* Emerging roles of nucleotide metabolism in cancer development: progress and prospect. *Aging (Albany NY)* **13**, 13349-13358 (2021). https://doi.org/10.18632/aging.202962

2 Mullen, N. J. & Singh, P. K. Nucleotide metabolism: a pan-cancer metabolic dependency. *Nature Reviews Cancer* **23**, 275-294 (2023). https://doi.org/10.1038/s41568-023-00557-7

3 Burrell, R. A., McGranahan, N., Bartek, J. & Swanton, C. The causes and consequences of genetic heterogeneity in cancer evolution. *Nature* **501**, 338-345 (2013). https://doi.org/10.1038/nature12625

4 Ceppi, P. *et al.* Squamous cell carcinoma of the lung compared with other histotypes shows higher messenger RNA and protein levels for thymidylate synthase. *Cancer* **107**, 1589-1596 (2006). https://doi.org/https://doi.org/10.1002/cncr.22208

5 Monica, V. *et al.* Differential Thymidylate Synthase Expression in Different Variants of Large-Cell Carcinoma of the Lung. *Clinical Cancer Research* **15**, 7547-7552 (2009). https://doi.org/10.1158/1078-0432.Ccr-09-1641

6 Monterisi, S. *et al.* Solute exchange through gap junctions lessens the adverse effects of inactivating mutations in metabolite-handling genes. *Elife* **11** (2022). https://doi.org/10.7554/eLife.78425

7 Wu, F. *et al.* Single-cell profiling of tumor heterogeneity and the microenvironment in advanced non-small cell lung cancer. *Nature Communications* **12**, 2540 (2021). https://doi.org/10.1038/s41467-021-22801-0

8 Fontana, R., Mestre-Farrera, A. & Yang, J. Update on Epithelial-Mesenchymal Plasticity in Cancer Progression. *Annu Rev Pathol* **19**, 133-156 (2024). https://doi.org/10.1146/annurev-pathmechdis-051222-122423

9 Wang, L., Lankhorst, L. & Bernards, R. Exploiting senescence for the treatment of cancer. *Nature Reviews Cancer* **22**, 340-355 (2022). https://doi.org/10.1038/s41568-022-00450-9

10 Park, S. S., Choi, Y. W., Kim, J.-H., Kim, H. S. & Park, T. J. Senescent tumor cells: an overlooked adversary in the battle against cancer. *Experimental & Molecular Medicine* **53**, 1834-1841 (2021). https://doi.org/10.1038/s12276-021-00717-5

11 Galanos, P. *et al.* Chronic p53-independent p21 expression causes genomic instability by deregulating replication licensing. *Nature Cell Biology* **18**, 777-789 (2016). https://doi.org/10.1038/ncb3378

12 Sprenger, H.-G. *et al.* Cellular pyrimidine imbalance triggers mitochondrial DNA–dependent innate immunity. *Nature Metabolism* **3**, 636-650 (2021). https://doi.org/10.1038/s42255-021-00385-9

13 Mackenzie, K. J. *et al.* cGAS surveillance of micronuclei links genome instability to innate immunity. *Nature* **548**, 461-465 (2017). https://doi.org/10.1038/nature23449

14 Motwani, M., Pesiridis, S. & Fitzgerald, K. A. DNA sensing by the cGAS-STING pathway in health and disease. *Nat Rev Genet* **20**, 657-674 (2019). https://doi.org/10.1038/s41576-019-0151-1

15 Donne, R. *et al.* Replication stress triggered by nucleotide pool imbalance drives DNA damage and cGAS-STING pathway activation in NAFLD. *Developmental Cell* **57**, 1728-1741.e1726 (2022). https://doi.org/10.1016/j.devcel.2022.06.003

16 Gehring, H. & Schröder, A. Thymidine secretion by cultured chicken embryo fibroblasts and NIH/3T3 cells: quantification and time course. *Biochem Biophys Res Commun* **177**, 259-264 (1991). https://doi.org/10.1016/0006-291x(91)91976-j

17 Fukasawa, M., Bryant, S. M. & diZerega, G. S. Incorporation of thymidine by fibroblasts: Evidence for complex regulation by postsurgical macrophages. *Journal of Surgical Research* **45**, 460-466 (1988). https://doi.org/https://doi.org/10.1016/0022-4804(88)90196-5

18 Orita, H., Campeau, J. D., Nakamura, R. M. & diZerega, G. S. Modulation of fibroblast proliferation and transformation by activated macrophages during postoperative peritoneal reepithelialization. *American Journal of Obstetrics and Gynecology* **155**, 905-911 (1986). https://doi.org/https://doi.org/10.1016/S0002-9378(86)80048-5

19 Halbrook, C. J. *et al.* Macrophage-Released Pyrimidines Inhibit Gemcitabine Therapy in Pancreatic Cancer. *Cell Metab* **29**, 1390-1399.e1396 (2019). https://doi.org/10.1016/j.cmet.2019.02.001

20 Simon, A. M. & Goodenough, D. A. Diverse functions of vertebrate gap junctions. *Trends in Cell Biology* **8**, 477-483 (1998). https://doi.org/10.1016/S0962-8924(98)01372-5

21 Goodenough, D. A. & Paul, D. L. Gap Junctions. *Cold Spring Harbor Perspectives in Biology* **1** (2009). https://doi.org/10.1101/cshperspect.a002576

22 Zhang, C. & Schekman, R. Syncytin-mediated open-ended membrane tubular connections facilitate the intercellular transfer of cargos including Cas9 protein. *eLife* **12**, e84391 (2023). https://doi.org/10.7554/eLife.84391

23 Platt, Randall J. *et al.* CRISPR-Cas9 Knockin Mice for Genome Editing and Cancer Modeling. *Cell* **159**, 440-455 (2014). https://doi.org/10.1016/j.cell.2014.09.014

24 Jackson, E. L. *et al.* Analysis of lung tumor initiation and progression using conditional expression of oncogenic K-ras. *Genes & Development* **15**, 3243-3248 (2001). https://doi.org/10.1101/gad.943001

25 Lee, S. M. *et al.* First-line atezolizumab monotherapy versus single-agent chemotherapy in patients with non-small-cell lung cancer ineligible for treatment with a platinum-containing regimen (IPSOS): a phase 3, global, multicentre, open-label, randomised controlled study. *The Lancet* **402**, 451-463 (2023). https://doi.org/https://doi.org/10.1016/S0140-6736(23)00774-2

26 Waldman, A. D., Fritz, J. M. & Lenardo, M. J. A guide to cancer immunotherapy: from T cell basic science to clinical practice. *Nature Reviews Immunology* **20**, 651-668 (2020). https://doi.org/10.1038/s41577-020-0306-5

27 Cadenas-De Miguel, S., Lucianer, G. & Elia, I. The metabolic cross-talk between cancer and T cells. *Trends in Biochemical Sciences* **48**, 597-609 (2023). https://doi.org/10.1016/j.tibs.2023.03.004

28 Reinfeld, B. I. *et al.* Cell-programmed nutrient partitioning in the tumour microenvironment. *Nature* **593**, 282-288 (2021). https://doi.org/10.1038/s41586-021-03442-1

29 Lyssiotis, C. A. & Kimmelman, A. C. Metabolic Interactions in the Tumor Microenvironment. *Trends Cell Biol* **27**, 863-875 (2017). https://doi.org/10.1016/j.tcb.2017.06.003

30 Hensley, Christopher T. *et al.* Metabolic Heterogeneity in Human Lung Tumors. *Cell* **164**, 681-694 (2016). https://doi.org/10.1016/j.cell.2015.12.034

31 Ackerman, D. & Simon, M. C. Hypoxia, lipids, and cancer: surviving the harsh tumor microenvironment. *Trends in Cell Biology* **24**, 472-478 (2014). https://doi.org/https://doi.org/10.1016/j.tcb.2014.06.001

32 Kumari, S., Advani, D., Sharma, S., Ambasta, R. K. & Kumar, P. Combinatorial therapy in tumor microenvironment: Where do we stand? *Biochimica et Biophysica Acta (BBA) -*

Reviews on Cancer **1876**, 188585 (2021). https://doi.org/https://doi.org/10.1016/j.bbcan.2021.188585

33 Mannherz, W. & Agarwal, S. Thymidine nucleotide metabolism controls human telomere length. *Nature Genetics* **55**, 568-580 (2023). https://doi.org/10.1038/s41588-023-01339-5

34 Aird, K. M. & Zhang, R. Nucleotide metabolism, oncogene-induced senescence and cancer. *Cancer Letters* **356**, 204-210 (2015). https://doi.org/https://doi.org/10.1016/j.canlet.2014.01.017

35 Schmitt, C. A., Wang, B. & Demaria, M. Senescence and cancer — role and therapeutic opportunities. *Nature Reviews Clinical Oncology* **19**, 619-636 (2022). https://doi.org/10.1038/s41571-022-00668-4

36 Wilson, P. M., Danenberg, P. V., Johnston, P. G., Lenz, H. J. & Ladner, R. D. Standing the test of time: targeting thymidylate biosynthesis in cancer therapy. *Nat Rev Clin Oncol* **11**, 282-298 (2014). https://doi.org/10.1038/nrclinonc.2014.51

37 Van Triest, B., Pinedo, H. M., Giaccone, G. & Peters, G. J. Downstream molecular determinants of response to 5-fluorouracil and antifolate thymidylate synthase inhibitors. *Ann Oncol* **11**, 385-391 (2000). https://doi.org/10.1023/a:1008351221345

38 Takezawa, K. *et al.* Thymidylate synthase as a determinant of pemetrexed sensitivity in non-small cell lung cancer. *Br J Cancer* **104**, 1594-1601 (2011). https://doi.org/10.1038/bjc.2011.129

39 Kim, G., Shin, H. M. & Kim, H.-R. Pyrimidine nucleotide starvation induces a decrease in the number of effector T cells but not memory T cells. *Cellular & Molecular Immunology* **20**, 859-860 (2023). https://doi.org/10.1038/s41423-023-01014-z

40 Lewis, J. R. Carbenoxolone sodium in the treatment of peptic ulcer. A review. *Jama* **229**, 460-462 (1974).

41 Sciacovelli, M. *et al.* Fumarate is an epigenetic modifier that elicits epithelial-to-mesenchymal transition. *Nature* **537**, 544-547 (2016). https://doi.org/10.1038/nature19353

42 Krieg, S., Fernandes, S. I., Kolliopoulos, C., Liu, M. & Fendt, S.-M. Metabolic Signaling in Cancer Metastasis. *Cancer Discovery* **14**, 934-952 (2024). https://doi.org/10.1158/2159-8290.Cd-24-0174

43 Shaul, Yoav D. *et al.* Dihydropyrimidine Accumulation Is Required for the Epithelial-Mesenchymal Transition. *Cell* **158**, 1094-1109 (2014). https://doi.org/https://doi.org/10.1016/j.cell.2014.07.032

44 Siddiqui, A. *et al.* Thymidylate synthase maintains the de-differentiated state of triple negative breast cancers. *Cell Death & Differentiation* **26**, 2223-2236 (2019). https://doi.org/10.1038/s41418-019-0289-6

45 Li, Q. *et al.* Thymidine kinase 1 drives hepatocellular carcinoma in enzyme-dependent and -independent manners. *Cell Metabolism* **35**, 912-927.e917 (2023). https://doi.org/https://doi.org/10.1016/j.cmet.2023.03.017

46 Siddiqui, M. A. *et al.* Thymidylate synthase drives the phenotypes of epithelial-to-mesenchymal transition in non-small cell lung cancer. *British Journal of Cancer* **124**, 281-289 (2021). https://doi.org/10.1038/s41416-020-01095-x

47 Siddiqui, A. *et al.* Thymidylate synthase is functionally associated with ZEB1 and contributes to the epithelial-to-mesenchymal transition of cancer cells. *J Pathol* **242**, 221-233 (2017). https://doi.org/10.1002/path.4897

48 Sahu, U. *et al.* Pyrimidines maintain mitochondrial pyruvate oxidation to support de novo lipogenesis. *Science* **383**, 1484-1492 (2024). https://doi.org/doi:10.1126/science.adh2771

49 Skinner, O. S. *et al.* Salvage of ribose from uridine or RNA supports glycolysis in nutrient-limited conditions. *Nature Metabolism* **5**, 765-776 (2023). https://doi.org/10.1038/s42255-023-00774-2

50 Tabata, S. *et al.* Thymidine Catabolism as a Metabolic Strategy for Cancer Survival. *Cell Reports* **19**, 1313-1321 (2017). https://doi.org/https://doi.org/10.1016/j.celrep.2017.04.061

51 Nwosu, Z. C. *et al.* Uridine-derived ribose fuels glucose-restricted pancreatic cancer. *Nature* **618**, 151-158 (2023). https://doi.org/10.1038/s41586-023-06073-w

52 Lee, H. J. *et al.* Conformational changes in the human Cx43/GJA1 gap junction channel visualized using cryo-EM. *Nat Commun* **14**, 931 (2023). https://doi.org/10.1038/s41467-023-36593-y

53 Bienert, S. *et al.* The SWISS-MODEL Repository-new features and functionality. *Nucleic Acids Res* **45**, D313-d319 (2017). https://doi.org/10.1093/nar/gkw1132

54 Kim, S. *et al.* PubChem 2023 update. *Nucleic Acids Research* **51**, D1373-D1380 (2022). https://doi.org/10.1093/nar/gkac956

55 Bitencourt-Ferreira, G. & de Azevedo, W. F. in *Docking Screens for Drug Discovery* (ed Walter Filgueira de Azevedo Jr) 149-167 (Springer New York, 2019).

56 Adasme, M. F. *et al.* PLIP 2021: expanding the scope of the protein–ligand interaction profiler to DNA and RNA. *Nucleic Acids Research* **49**, W530-W534 (2021). https://doi.org/10.1093/nar/gkab294

57 Rosignoli, S. & Paiardini, A. Boosting the Full Potential of PyMOL with Structural Biology Plugins. *Biomolecules* **12**, 1764 (2022).

Extended Table 1. List of guideRNA Sequences

Species	Gene	#gRNA1	Sequence	vector
Human	*TYMS*	#1	ACCCTTCCAGAACACACGTT	pLentiCRISPR v2
Human	*TYMS*	#2	TGACAACCAAACGTGTGTTC	pLentiCRISPR v2
Human	*TYMS*	#3	CATCGAGCCACTGAAAATTC	pLentiCRISPR v2
Human	*TK1*	#1	CGCCTGCCTGCTCCGAGACG	pLentiCRISPR v2
Human	*TK1*	#2	CGCCTGCCTGCTCCGAGACG	pLentiCRISPR v2
Human	*TK1*	#3	GCTGCTGTAGCGAGTGTCTT	pLentiCRISPR v2
Human	*RRM1*	#1	TGAGAACCTTCCAGTCCCAT	pLentiCRISPR v2
Human	*DTYMK1*	#1	ATGCGTATCTGTCCACGACG	pLentiCRISPR v2
Human	*Control*	#1	GAATAGATTTGTCAGTTAGG	pLentiCRISPR v2
Mouse	*Kras*	#1	GCAGCGTTACCTCTATCGTA	ITR-U6-sgRNA(Kras)-U6-sgRNA(p53)-pEFS-EYFP-2A-Cre-shortPA-KrasG12D_HDRdonor-ITR
Mouse	*p53*	#1	GTGTAATAGCTCCTGCATGG	ITR-U6-sgRNA(Kras)-U6-sgRNA(p53)-pEFS-EYFP-2A-Cre-shortPA-KrasG12D_HDRdonor-ITR
Mouse	*Tyms*	#1	TCACAACCAAACGAGTGTTC	pLentiCRISPR v2; ITR-U6-sgRNA(Kras)-U6-

				sgRNA(p53)-U6-sgRNA(Ts#1)-U6-sgRNA(Ts#2)-U6-sgRNA(Tk#1)-U6-sgRNA(Tk1#2)-pEFS-EYFP-2A-Cre-shortPA-KrasG12D_HDRdonor-ITR
Mouse	*Tyms*	#2	ACCCTTCCAGAACACTCGTT	pLentiCRISPR v2; ITR-U6-sgRNA(Kras)-U6-sgRNA(p53)-U6-sgRNA(Ts#1)-U6-sgRNA(Ts#2)-U6-sgRNA(Tk#1)-U6-sgRNA(Tk1#2)-pEFS-EYFP-2A-Cre-shortPA-KrasG12D_HDRdonor-ITR
Mouse	*Tyms*	#3	TCACAACCAAACGAGTGTTC	pLentiCRISPR v2
Mouse	*Tk1*	#1	TAGGACTGACCGATCATGTG	pLentiCRISPR v2; ITR-U6-sgRNA(Kras)-U6-sgRNA(p53)-U6-sgRNA(Ts#1)-U6-sgRNA(Ts#2)-U6-sgRNA(Tk#1)-U6-sgRNA(Tk1#2)-pEFS-EYFP-2A-Cre-shortPA-KrasG12D_HDRdonor-ITR
Mouse	*Tk1*	#2	GCAGGCTGGCAATGCGTCCA	pLentiCRISPR v2; ITR-U6-sgRNA(Kras)-U6-

				sgRNA(p53)-U6-sgRNA(Ts#1)-U6-sgRNA(Ts#2)-U6-sgRNA(Tk#1)-U6-sgRNA(Tk1#2)-pEFS-EYFP-2A-Cre-shortPA-KrasG12D_HDRdonor-ITR
Mouse	*Tk1*	#3	TTCCCAGTTTCCTGACATTG	pLentiCRISPR v2
Mouse	*Tk1*	#4	TCCTTGGGTGTGGCCGTCAT	pLentiCRISPR v2

Extended Table 2. List of Antibodies

Antibody	Short Name	Molecular Weight (KDa)	Species	Blocking	Dilution	Supplier
Thymidylate Synthase	TS	36	human / mouse	5% milk	1:5000	Abcam
Thymidine Kinase 1	TK1	26	human	5% milk	1:2000	Cell Signaling
Ribonucleotide Reductase 1	RRM1	90	human / mouse	5% milk	1:1000	Cell Signaling
Deoxythymidylate Kinase	DTYMK	30	human / mouse	5% milk	1:1000	Abcam
Gap Junction Protein Alpha 1	GJA1 (Cx43)	43	human / mouse	5% milk	1:1000	Cell Signaling
Gap Junction Protein Delta 3	GJD3	30	human/mouse	5% milk	1:1000	Invitrogen
p21 Waf1/Cip1	p21	21	human/mouse	5% milk	1:1000	Cell Signaling
β-Actin (8H10D10)	β-Actin	42	human/mouse	5% milk	1:10000	Cell Signaling
phospho-STING	p-STING	40	Human/mouse	3% BSA	1:500	Cell Signaling
phospho-TBK1/NAK	p-TBK1	80	Human/mouse	3% BSA	1:500	Cell signaling
Anti-Rabbit Goat Secondary (HRP)					1:1000 - 1: 5000	Biolegend